2024

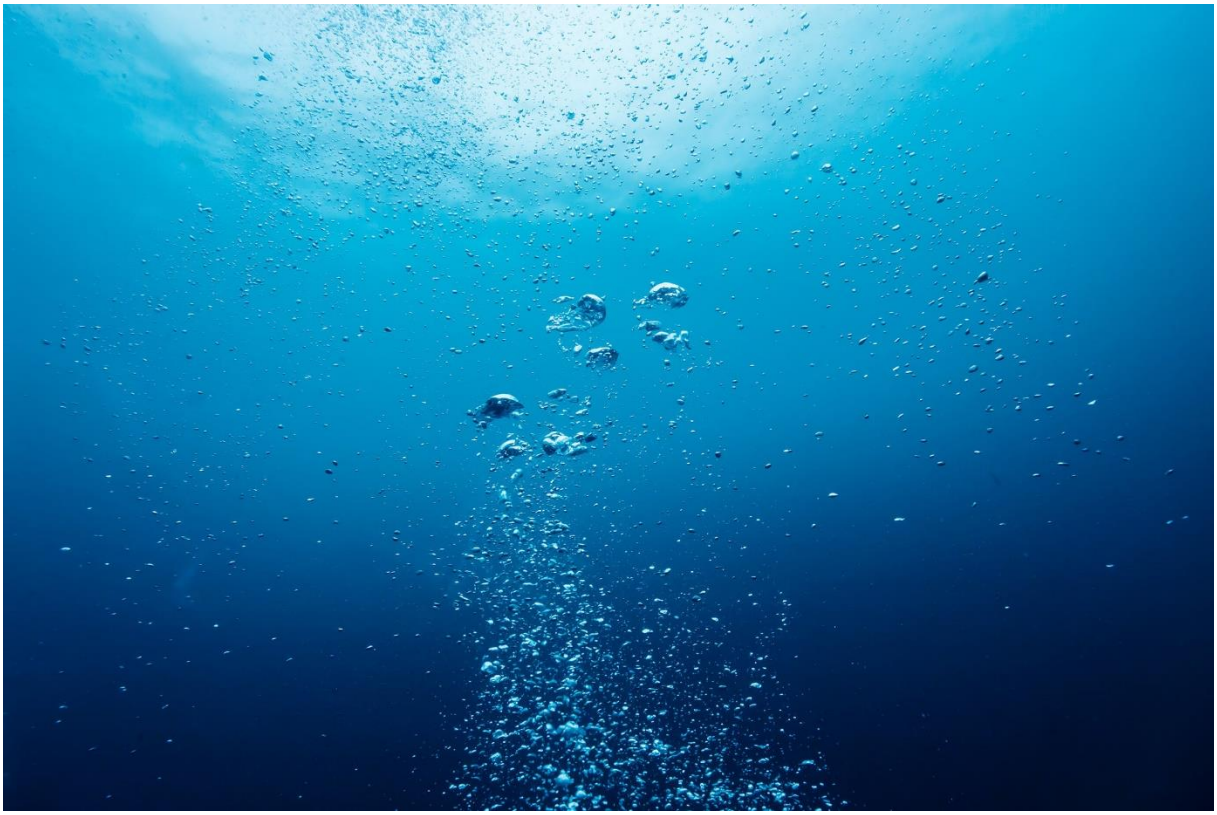

Anthropogenic carbon in the Atlantic Ocean at 40°S from 1972 to 2014

ANNE ROOZENDAAL

EARTH, LIFE AND CLIMATE

Abstract

The anthropogenic carbon (C_{ant}) concentration at 40°S in the Atlantic Ocean was calculated over the period 1972-2014. The C* method was used to eliminate the biological fraction of the total DIC, both AOU and NO_3 were used in the calculations. With the use of a multiple linear regression method the size of the oceanic CO_2 sink over this period was determined as 34.9 ± 3.19 mol m^{-2} for $C_{ant\text{-}AOU}$ and 35.9 ± 3.71 mol m^{-2} for $C_{ant\text{-}NO3}$. Roughly 100% of the total DIC increase over this period can be related to the increase in C_{ant} concentration. In the depth range where the products of organic matter remineralization are high on top of the C_{ant} increase, the decreased TA/DIC ratio results in an increased sensitivity for the pCO_2, pH and H^+ ions. The carbonate system acts as a whole and is altered upon additions of CO_2 to the surface ocean.

Index

1 Introduction

The global carbon cycle plays an important role in regulating the climate system. The Earth has three main carbon storage reservoirs of which the exchange rates are fast enough to fluctuate over decades: the atmosphere, the terrestrial biosphere and the ocean. The relative sizes of these reservoirs are: 1:5:60 (Sabine and Tanhua, 2010). Carbon dioxide (CO_2) is constantly added to the atmosphere, mainly through fossil fuel burning, and transferred to those reservoirs through complex reactions (Gruber et al., 2004) (Figure 1).

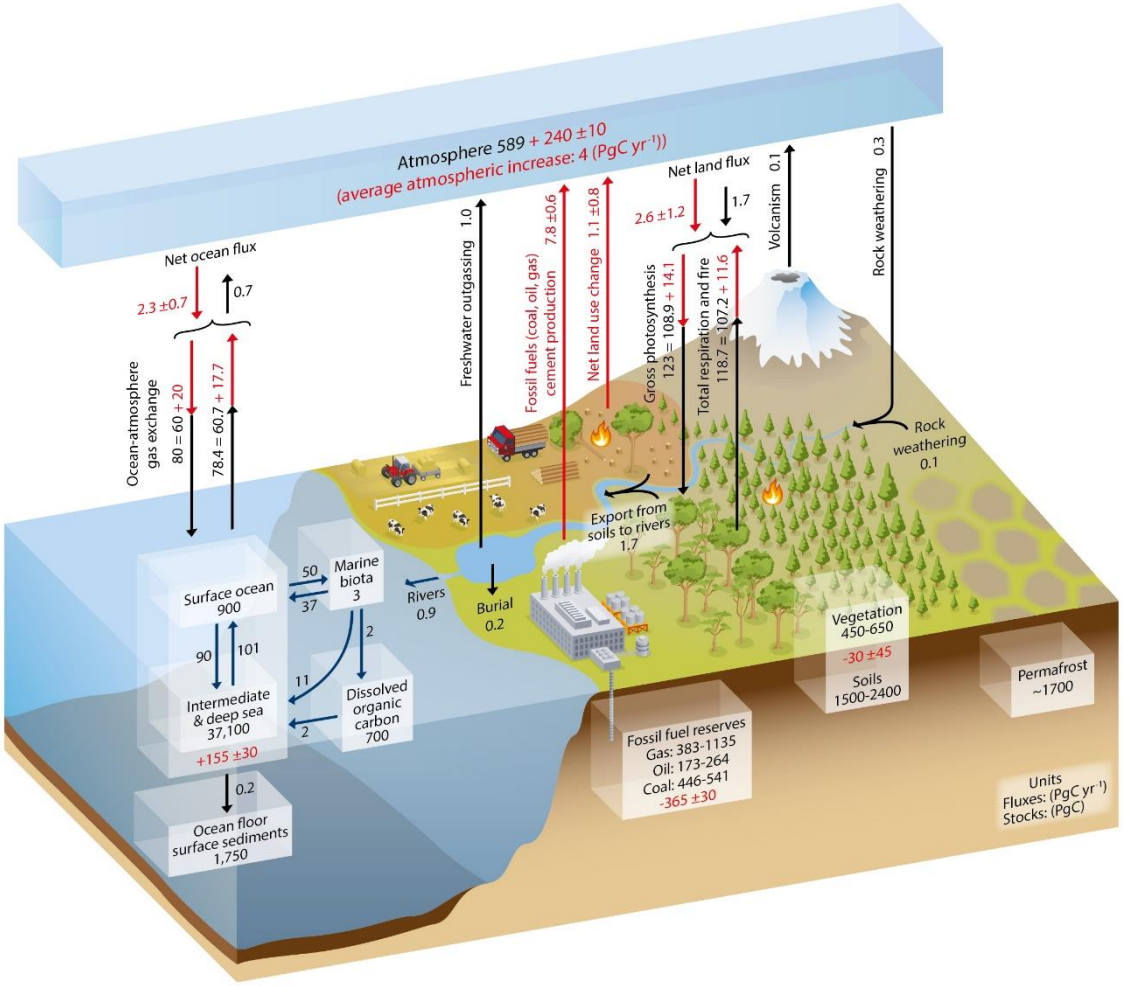

Figure 1: Schematic of the global carbon cycle. The magnitude of the different reservoirs is shown and the fluxes between them. In black are the fluxes that already existed before the industrial revolution and the red numbers show the anthropogenic perturbation. The red numbers are calculated from a mean over the period from 2000-2009. (IPCC 2013, chpt. 6, Ciais et al., 2013)

Since the Industrial Revolution the atmospheric CO_2 concentration has increased from ~283 in 1800 to over 418 ppm in 2022, which is the highest value in 3 million years (Trans and Keeling for NOAA, Berends et al., 2021). This extra inorganic carbon is added to the atmosphere in the form of CO_2(g) and is well mixed throughout the whole atmosphere (below 100 km) (Jacob, 1999). Fossil fuel burning, production of cement and agriculture account for 40% of this extra CO_2 called anthropogenic carbon (C_{ant}) (Gruber et al., 2019, Houghton et al., 2017). About 30% of this C_{ant} is dissolved and stored in the ocean (Gruber et al., 2019).The oceanic CO_2 uptake at the surface ocean is highest in the mid-latitudes and the high-latitude North Atlantic. Central, intermediate and deep water masses are formed at these locations, transporting anthropogenic carbon into the inner ocean

(Friedlingstein et al., 2022). Strong winds and low temperatures enhance the uptake at these locations (Takahashi et al., 2009).

This research is focused on a transect in the South Atlantic Ocean around latitude 40°S (Figure 3). This is an area of high primary productivity in the open ocean and therefore the biological pump (section 2.2) is active (Tuerena et al., 2019). In the subtropical gyre, north of the transect (Figure 2), the waters are macro-nutrient limited and iron-rich, while the Antarctic circumpolar current (ACC) is iron-limited but has high macro-nutrient concentrations, both resulting in unfavorable conditions for phytoplankton to grow (Browning et al., 2014). The subtropical convergence zone (STCZ) is the meeting point of the southwards flowing subtropical gyre waters and the northwards flowing ACC leading to a zone of high nutrient availability and phytoplankton growth. Figure 3 shows the locations of the stations around the transect that are used in this study.

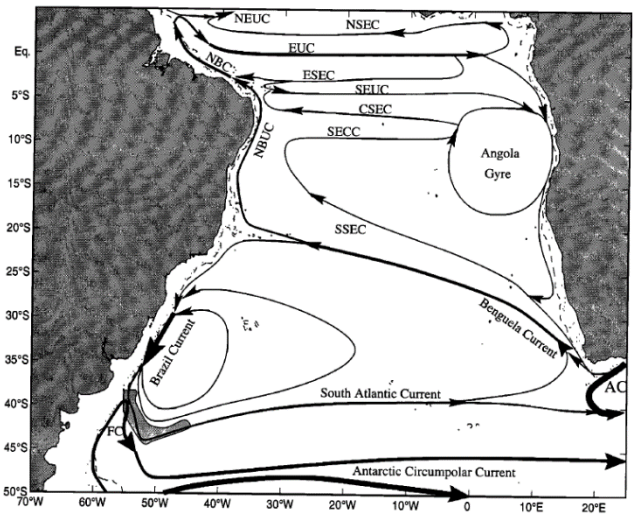

Figure 2: surface currents in the South Atlantic Ocean (Stramma and England, 1999)

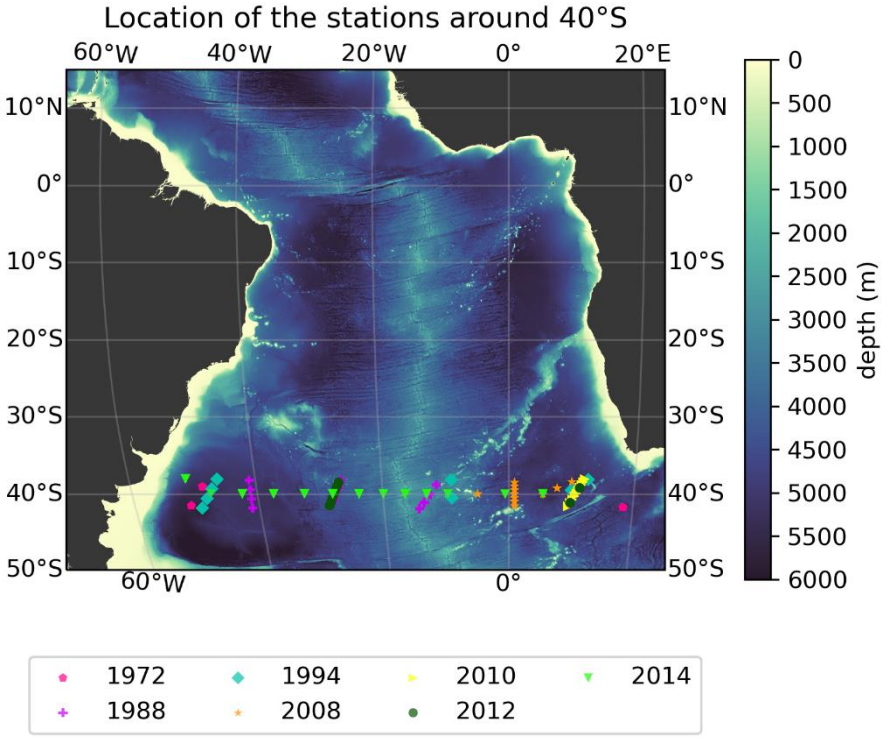

Figure 3: Station locations of the different cruises around the transect. The cruises that happened within the same year (or one year apart) were grouped together as one. The background color is the depth of the ocean in meters, made by making use of the GEBCO 2023 dataset.

The location of the transect at 40°S is an interesting region for carbonate chemistry. It is found at the border between the Atlantic Ocean and the Southern Ocean. Three main water masses in the Atlantic Ocean are found at the location of this transect (section 2.5), out of which the Antarctic Intermediate Water is formed slightly more south of the transect and carries a high concentration of

C_{ant} (Gruber et al., 2019). Because it is still largely unknown how the biological cycle and the rest of the ocean will react to an increasing C_{ant} concentration in the surface ocean, it is an interesting first step to a more complete understanding of the carbonate chemistry in the ocean to calculate the C_{ant} concentration at this transect.

In this research the effect of the increase in the C_{ant} concentration at 40°S on several carbonate system parameters will be calculated. The increase in C_{ant} concentration between 1972 and every following year with datapoints on the transect will be calculated by using a multiple linear regression method (MLR) in combination with the C* method. The increase in C_{ant} will be calculated for every water mass along the transect to see how the anthropogenic carbon distribution over depth has changed over time. The increase in DIC will be compared to the increase in C_{ant} over time and the influence of C_{ant} on pH, pCO_2 and H^+ ions will be discussed. Upon addition of C_{ant} to the ocean the relative change in CO_2 may not be equal to the change in DIC, this is expressed in the Revelle Factor (section 2.1). At last the increase in C_{ant} will be compared to the increase in the atmospheric pCO_2 concentration.

2 Background

2.1 Carbonate chemistry in the ocean

About 30% of anthropogenic carbon is dissolved and stored in the ocean. Dissolution takes place at the air-sea interface, according to the following reaction (Zeebe and Wolf-Gladrow, 2001):

$$CO_2(g) \rightleftharpoons CO_2(aq) \qquad \text{(Eq. 1)}$$

The time scale for equilibrium at the air-sea exchange is about one year (Jones et al., 2014). The rate at which global surface water $CO_2(aq)$ concentration increases is therefore closely synched with the atmospheric CO_2 concentration (Takahashi et al., 2009). Regionally, however, biological or physical processes can considerably alter the surface water CO_2 concentration.

Part of the dissolved CO_2 will react with water to form carbonic acid (Equation 3). This equilibrium occurs slowly, which means that almost all of the dissolved CO_2 will stay in the form $CO_2(aq)$. For convenience CO_2* is defined as the sum of aqueous CO_2 and carbonic acid:

$$CO_2^*(aq) = CO_2(aq) + H_2CO_3(aq) \qquad \text{(Eq. 2)}$$

Carbonic acid is a weak acid that will dissociate into a bicarbonate ion and a proton. Bicarbonate will then partly dissociate into a carbonate ion and a proton. Most of the $CO_2(aq)$ will react with carbonate ions to form bicarbonate.

$$CO_2^*(aq) + H_2O \rightleftharpoons HCO_3^- + H^+ \rightleftharpoons CO_3^{2-} + 2H^+ \qquad \text{(Eq. 3)}$$

With equilibrium constants K_1 and K_2, that are related to the concentrations:

$$K_1 = \frac{[HCO_3^-][H^+]}{[CO_2]} \qquad \text{(Eq. 4)}$$

$$K_2 = \frac{[CO_3^{2-}][H^+]}{[HCO_3^-]} \qquad \text{(Eq. 5)}$$

The different components of the carbonate system determine the seawater pH; at pH values below pK_1 the most protonated species, CO_2*(aq), is dominant (Figure 4). When the pH is higher than the pK_2 the least protonated species, the carbonate ion, is dominant. Between pK_1 and pK_2 the bicarbonate ion is dominant (Figure 4) (as reviewed by Middelburg 2019). At typical open ocean seawater conditions of S ≈35 and pH ≈8, bicarbonate is the dominant species and makes up ~90% of the total dissolved inorganic carbon, the carbonate ion makes up ~9% and only ~1% is CO_2*(Zeebe and Wolf-Gladrow, 2001, Middelburg, 2019).

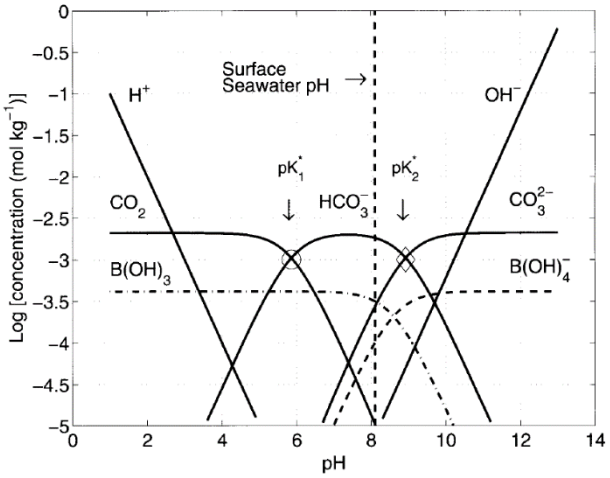

Figure 4: Bjerrum plot of the carbonate system, DIC=2.1 mmol kg^{-1}, S=35 and T= 25 C. The circle and the diamond indicate the equivalence points (Zeebe and Wolf-Gladrow, 2001)

The values of the equilibrium constants are dependent on temperature (T), pressure (P) and salinity (S); a decreasing T, P and S (with respect to the reference of T=25°C, S= 35 and P=1 atm) will increase the p*K* values and thus the relative proportions of the different carbon species will shift towards more protonated species. The effect of an increase in pressure is less pronounced (Zeebe and Wolf-Gladrow, 2001). Species with a higher charge are more sensitive to changes in salinity than species with a lower charge, with an increasing salinity the p*K* value will decrease.

The sum of the total concentration of aqueous CO_2, HCO_3^-, and CO_3^{2-} in a solution make up total dissolved inorganic carbon species (DIC):

$$DIC = [CO_2^*] + [HCO_3^-] + [CO_3^{2-}] \quad \text{(Eq. 6)}$$

The pCO_2 is the partial pressure of CO_2 in the gas phase, which is in equilibrium with the dissolved CO_2 in the seawater. The net air-sea CO_2 exchange can be estimated from the difference between the pCO_2 in the ocean and the pCO_2 in the atmosphere (Zeebe and Wolf-Gladrow, 2001).

Alkalinity can be described as the excess of proton acceptors over proton donors relative to a defined zero level of protons (ZLP) (Dickson, 1981). In other words, it is the acid neutralization capacity of a medium. The most dominant proton acceptors in the ocean are the carbonate ion, bicarbonate ion, boric acid and the hydroxide ion. Alkalinity also includes minor species that only become important at extreme pH values (Zeebe and Wolf-Gladrow, 2001). The following simplified equation includes >99.8 of its total elements (Humphreys et al., 2018). The carbonate ion is counted twice because it can absorb two protons to reach the ZLP:

$$TA = [HCO_3^-] + 2[CO_3^{2-}] + [B(OH)_4^-] + [OH^-] - [H^+] \text{ (+ minor components)} \quad \text{(Eq. 7)}$$

Alkalinity can also be described in terms of conservative ions; the sum of the major cations, Na^+, K^+, Mg^{2+} and Ca^{2+} in seawater is not fully compensated by the sum of the major anions, Cl^- and SO_4^{2-}. This small imbalance in charge is responsible for the alkalinity in the ocean and is mainly compensated by the anions of the carbonate system. The charge difference fluctuates upon salinity changes that mainly happen in the surface ocean. The composition of conservative ions does not change upon addition or removal of CO_2 to the ocean, meaning that the alkalinity will stay constant (Figure 5). The concentration of conservative ions does change due to precipitation or dissolution of $CaCO_3$, changing the alkalinity by 2 mol per mol $CaCO_3$ (Zeebe and Wolf-Gladrow, 2001).

Following Wolf-Gladrow et al. (2007), all the nutrients in the alkalinity expression can be grouped together as a nitrate unit. To do this a constant Redfield Ratio (Equation 14) is assumed for the

contribution of the different nutrients to the TA, the Redfield Ratio of NO_3^-:PO_4^-:SO_4^{2-} is 16 :1 :2.4 is used. The increase in TA when 1 mole of organic matter is dissolved is:

$$\Delta TA = 2 \cdot CO_3^{2-} - \frac{(16 + 1 + 2 \cdot 2.4)}{16} \cdot NO_3^- = 2 \cdot CO_3^{2-} - 1.36 \cdot NO_3 \qquad \text{(Eq. 8)}$$

Sulfate is counted twice in Dickson's definition for alkalinity, the extended version of equation 7 (see appendix 1), because two protons can be absorbed before reaching the ZLP.

Figure 5 shows the effect of different processes on the TA, DIC, pH and CO_2*. With the invasion of CO_2 into the ocean the TA remains unchanged and the DIC increases. As a response to the increase in CO_2* concentration in the ocean the carbonate speciation changed, decreasing the pH. Release of CO_2 to the atmosphere would lead to the opposite effect.

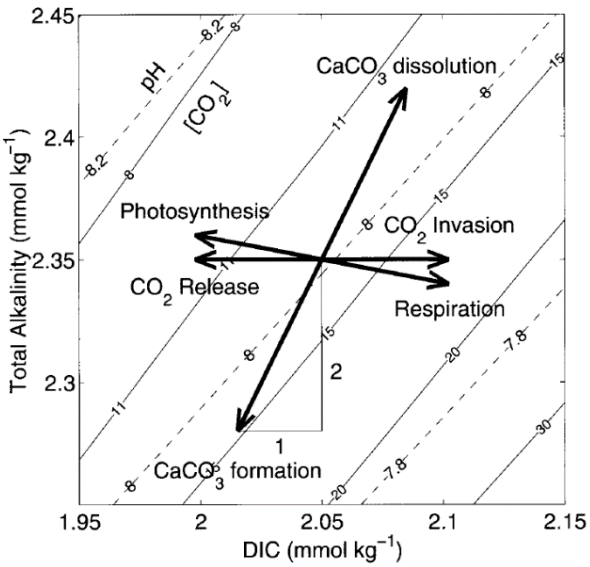

Figure 5: The effect of different processes on the DIC, TA and pH (Zeebe and Wolf-Gladrow, 2001)

The buffer capacity (Equation 9) is the amount of acid or base that can be neutralized by the solution so the pH does not change drastically. In a solution that is pure water, the buffer capacity is high at a very low or very high pH, where either the H^+, or the OH^- concentration is very small, because that is then all bound to the acid or base that is added. In the pH range where the buffer capacity is high, the pH changes relatively little. In a weak acid or base solution, like the ocean, there is another pH range where the pH change is relatively small, this is where the pH is equal to the equilibrium constant. Enough species in the solution can accept a proton to neutralize the change in pH.

$$\beta = \frac{d[acid]}{d\ pH} \qquad \text{(Eq. 9)}$$

In seawater the buffer capacity is highest at a pH of ~9, mostly due to the ions in the carbonate system (Figure 6). When the buffer capacity is high, the speciation of the weak acid changes, meaning that the fraction of the weak acid and its conjugate base is about equal. When the ratio of the acid and its conjugate base is out of balance, the weak acid is 'completely used up' and the pH will change drastically upon addition of more acid. Acidification causes the pH to move further away from the p*K* value, hereby decreasing the buffer capacity and carbonate ion concentration. This is one of the reasons why less CO_2 can be taken up by the ocean without causing a change in pH (as reviewed by Middelburg 2019, Zeebe and Wolf-Gladrow, 2001).

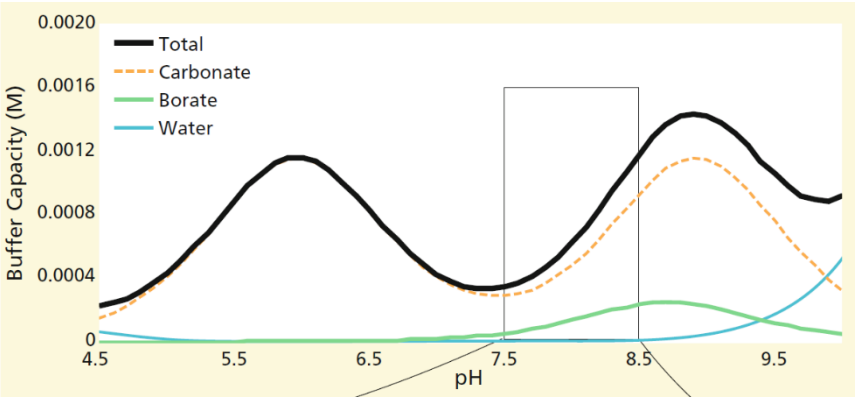

Figure 6: Buffer capacities of different components in seawater (Middelburg et al., 2019)

The carbonate system, in combination with the boron compounds serves as a pH buffer in the ocean. The response of the system to the uptake of CO_2 is expressed in terms of relative changes in CO_2 and DIC that make up the Revelle factor. As the CO_2 concentration in the ocean increases, the speciation of the different carbonate species changes and the pH decreases. Where the CO_2 and HCO_3^- concentrations increase, the CO_3^{2-} concentration decreases. This shows that the increase in DIC is not equal to the increase in CO_2. The Revelle Factor is given in equation 10, assuming constant alkalinity:

$$RF = \frac{d[CO2]}{[CO2]} / \frac{dDIC}{DIC} \qquad \text{(Eq. 10)}$$

The relative increase in CO_2 is larger than the increase in DIC upon the addition of CO_2 to the ocean, meaning that the Revelle Factor will increase (Zeebe and Wolf-Gladrow, 2001). With an increasing Revelle Factor the buffer capacity will decrease and therefore the sink efficiency is expected to decrease (Jiang et al., 2019).

With any two given parameters of the CO_2 system, the rest can be calculated via mass balance and equilibrium equations. However, not all parameters can be measured directly from seawater and thus always have to be calculated (Zeebe and Wolf-Gladrow, 2001).

2.2 Biological pump

The carbon pump is the process that transports CO_2 from the surface ocean into the ocean interior. The carbon pump can be separated into a solubility pump and a biological pump, of which the latter can be split up into a soft tissue pump and a carbonate pump.

More than 50% of global primary production occurs in the surface ocean by marine microorganisms (Müller-Karger et al. 2005). With their large variety and exceptional abundance marine microorganisms play an important role in regulating the climate (Das and Mangwani, 2015). DIC and nutrients are used to build organic carbon in the surface ocean (Equation 11) (Figure 7, POC and DOC) and when this is transported into the deep sea the organic carbon is decomposed and DIC and nutrients are released back into the water column (reverse of equation 11). The biological pump essentially transports inorganic and organic carbon against the vertical DIC gradient into the deep ocean (Figure 7, PIC, POC, DOC are remineralized into DIC) (Sarmiento and Gruber, 2006). The formation of organic matter lowers the atmospheric CO_2 concentration locally by lowering the DIC in surface waters, causing atmospheric CO_2 to infiltrate the water (Equation 11). The soft tissue pump is the part of the biological pump that transports organic carbon from the surface into the deep ocean and contributes the largest part to the DIC (Figure 7, POC+DOC→DIC). The carbonate pump represents the precipitation and dissolution (at depth) of $CaCO_3$ (Sigman and Hain 2012). The formation of carbonate minerals locally increases the CO_2 concentration (Equation 12).

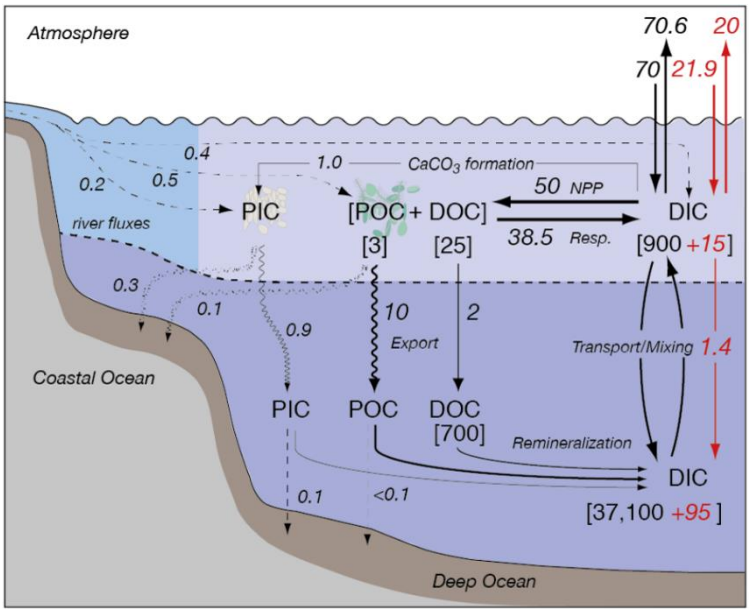

Figure 7: Biological activity regulates the organic and inorganic carbon pathways in the surface ocean. Like in figure 1 the red numbers show the anthropogenic carbon contribution while the black arrows show the natural fluxes. A net uptake of anthropogenic CO2 of 1.9 Pg C yr^{-1} is visible at the ir-sea interface (Sabine et al., 2004, Clement, 2018)

$$CO_2 + H_2O \rightleftharpoons CH_2O + O_2 \quad \text{(Eq. 11)}$$

$$Ca^{2+} + 2HCO_3^- \rightleftharpoons CaCO_3 + CO_2 + H_2O \quad \text{(Eq. 12)}$$

Marine plankton take up nutrients in an atomic ratio of C:N:P:O 106: 16: 1: -170 (Equation 13) (Redfield et al., 1963, Johnson et al., 2022).

$$106\ CO_2 + 16\ HNO_3 + H_3PO_4 + 122\ H_2O \rightleftharpoons (CH_2O)_{106}(NH_3)_{16}H_3PO_4 + 170\ O_2 \quad \text{(Eq. 13)}$$

This reaction can be extended by other elements that can be important, depending on the application. The equation shows that 170 moles of oxygen are used to degrade 1 mole of organic matter and 16 moles of nitrate, 106 moles of carbon and 1 mole of phosphate are released. The elemental ratio shown is equation 13 changes lattitudally and per ecosystem. The warm, nutrient-depleted gyre waters for example vary significantly from the cold, nutrient-rich waters in the high latitudes (Martiny et al., 2013). Assuming that oxygen saturation was reached when the water mass was at the surface, the apparent oxygen utilization (AOU) can be calculated:

$$AOU = O_2^{sat} - O_2^{measured} \quad \text{(Eq. 14)}$$

The oxygen defict can be used to calculate the original organic matter concentration, assuming a constant Redfield Ratio over time and depth. Because the different nutrients are found in constant ratios, the original organic matter concentration can also be calculated by the increase in nutrient concentrations.

$CaCO_3$ produced in the surface layer can settle down to the ocean interior and either accumulate on the sea floor or dissolve (Equation 12). The solubility of calcium carbonate increases with a decrease in temperature and an increase in pressure. Carbonate solubility therefore increases with depth, partly due to thermodynamics and partly as a result of respiration of organic matter (the soft tissue pump) (Boudreau et al. 2018, Boudreau et al. 2010). If the waters were to resurface in equatorial regions, the water column would degas as a consequence of the warming of the waters and the resulting decrease in solubility.

At the carbonate compensation depth (CCD) the particle settling rate is equal to the dissolution rate; below the CCD the dissolution rate is higher than the sedimentation rate and the sediments here will be carbonate-free. During periods of ocean acidification the CCD will rise on a short timescale due to the reduced carbonate flux. But on the long term the CCD would deepen because the carbonate enriched waters from the surface will reach the deep ocean and that will reduce the dissolution (Boudreau et al. 2018).

2.3 Solubility pump

The physical CO_2 uptake by the ocean is controlled by the large scale overturning circulation. Surface water flows from the equator towards the poles losing heat on its way due to the temperature gradient with the overlaying air. Once the water mass has arrived at the poles its density has increased due to cooling and evaporation, which increases the salinity. This high density water sinks at the poles and is transported into the deep ocean. As long as the water is in contact with the atmosphere, it can exchange CO_2, which can then be transported into the ocean interior at locations of deep water formation (Rahmsorf, 2002, Wunsch, 2002). Cold, deep waters are enriched in DIC this is because the solubility of CO_2 increases with decreasing temperatures. The storage rates of (anthropogenic) carbon vary spatially over the world and are highest at locations of deep water formation. Due to the slow mixing into the ocean interior and the few locations of deep water formation, the spatial spread of anthropogenic carbon is limited (Sabine et al., 2010).

2.4 Future scenarios for the carbon pump

The upward flux from the deep ocean, carrying nutrients, declines globally as a result of increasing temperatures and freshening of the surface ocean. This decreases the density and makes the water mass less prone to sinking, weakening the overturning circulation. Primary production decreases as a consequence of the limited nutrient availability. This decreases the vertical DIC gradient and essentially reduces the CO_2 uptake (Yamamoto et al., 2017). Under nutrient stress smaller phytoplankton are preferred over larger ones due to their relatively larger surface area through which the uptake of nutrients is more efficient. The sinking particulate carbonate flux decreases as a result of this community shift, also because the export of smaller sized particles is less powerful (Fu et al., 2016). Moreover, the balance between autotrophic and heterotrophic organisms is predicted to change. Consequently, increased recycling and respiration in warmer water causes the DIC to be retained in the surface waters thus potentially decreasing the biological pump (Wohlers et al., 2009).

Next to the increase in temperatures, the surface water density will be further decreased by an intensified hydrological cycle, bringing more fresh water to the surface ocean and further weakening the overturning circulation (Troggweiler and Russell, 2008). This results in a reduced CO_2 uptake at high latitudes. The weaker equatorial upwelling has an opposite result: the uptake of CO_2 is increased here as a result of the decreased upward carbon transport (Yamamoto et al., 2017, Sallée et al., 2021). The reduced carbonate export related to the reduced nutrient supply to the surface ocean is predicted to dominate, overall decreasing the carbon export (Zickfeld et al., 2008).

Due to the increased pCO_2 in the surface ocean and the coupled decrease in pH, the concentration of the carbonate ion decreases while the bicarbonate ion concentration increases (Equation 3). Marine calcifying organisms have to overcome the challenge of enhanced dissolution because the water can become under-saturated with respect to $CaCO_3$ (Das and Mangwani, 2015). Especially at higher latitudes where the $CaCO_3$ saturation is lower which results in $CaCO_3$ undersaturation after a slight decrease in pH (Orr et al., 2005 in Sabine et al., 2010). It is hard to predict how the community will change upon increasing anthropogenic carbon concentrations because the response towards acidification is species-specific, but the community structure will change (Price et al., 2007, Dutkiewicz et al., 2015). A model study by Dutkiewicz et al. (2015) shows that the effect of acidification on the ecological function of the plankton community had a greater impact than reduced nutrient supply or warming.

2.5 Water mass description

In this study neutral density levels (γ) are used to look at the depth in the ocean instead of looking at the depth in meters. Neutral density levels are a function of pressure, temperature and salinity but also of longitude and latitude and it accurately approximates isopycnal surfaces (Jackett and McDougall, 1997). Because water masses in the deep ocean flow along these isopycnal surfaces it is more robust to describe things along neutral surfaces instead of depth.

The South Atlantic Ocean can be vertically divided into four main layers. South Atlantic Central Water (SACW) is located in the South Atlantic current which comprises the southernmost part of the subtropical gyre. The subtropical gyre flows between 15°S and 40°S (Figure 2) and brings warm tropical surface waters southwards in the Brazil current. The surface waters in the transect are composed of SACW with a neutral density level of $26.0 < \gamma < 27.5$ kg m-3 (Figure 8) (Liu and Tanhua, 2020). The SACW is relatively warm and nutrient-poor compared to the Antarctic Intermediate Water (AAIW) that is found underneath (Stramma and England, 1999). Central waters have a linear T-S relationship, with low nutrient concentrations. They are commonly subducted below the thermocline and during winter they are formed in a subsurface layer with uniform densities (Stramma and England, 1999). Vertically central waters formed in the East Atlantic are found below central waters formed in the West Atlantic. The lower part of central waters can be described by mode water. The

transport and formation of mode and central waters are influenced by surface currents (Liu and Tanhua, 2021).

The Atlantic Ocean receives water from the Indian Ocean through Agulhas intrusions. Agulha leakage around the southern edge of Africa carries warm, saline water from the Indian Ocean into the Atlantic Ocean. The Agulhas escape from the western boundary current in the Indian Ocean (Beal et al., 2011). This Indian Ocean water contributes to the upper layers of the Atlantic Ocean and makes the eastern part of the basin more nutrient-rich (Liu and Tanhua, 2021).

Due to the increasing temperatures on earth more and more Antarctic melt water will enter the ocean. Ocean water close to Antarctica is generally macro-nutrient loaded but the primary productivity is low. this could be explained by strong wind forcing and sediment rich melt water input that result in turbid waters (Schloss et al., 2012). Glaciers terminating on land transport sediment-laden meltwater to the ocean and result in turbid waters where the light penetration is limited, reducing the primary production. The nutrient concentration remains therefore higher in the waters transported to the Southern Ocean and South Atlantic which may result in higher primary production and carbon uptake there (Jones et al., 2023). As more glaciers will end on land in the future, the nutrient fluxes in the Southern Ocean may change.

AAIW is found below the SACW and is formed in the densest part of the southern Subantarctic zone between 55°S and 40°S (Figure 8). The AAIW is found between 500 and 1200m and carries low salinity (34.206±0.083) water northwards along the continental slope (Talley, 1996, Liu and Tanhua, 2021). The water mass is formed in surface regions of the ACC, and contains a high oxygen(300.7±16.2 µmol m^{-3}) and a relatively low silicate concentration (21.09±4.66 µmol m^{-3}). Intermediate water from the Indian Ocean may also contribute to the South Atlantic AAIW through Agulhas leakage (Liu and Tanhua, 2021, Stramma and England, 1999). The AAIW has a neutral density surface of 26.95 < γ < 27.50 kg m-3 (Liu and Tanhua, 2021).

Underneath the AAIW the North Atlantic Deep Water (NADW) is found, this water mass flows southward (Figure 9) and is formed by deep water formation in the North Atlantic with a density of 27.85 < γ < 28.10 kg m-3 the water mass is found between 1500 and 3500 m depth (Liu and Tanhua, 2021). The water mass is transported into the southern hemisphere by the deep western boundary current. Depending on how far north the water was formed the water flows at a deeper level (Stramma and England, 1999). The water mass can be found all the way south to 50°S where it mixes with the Antarctic bottom waters (Liu and Tanhua, 2021). NADW can be identified as a water mass with a very high oxygen concentration (278.0±4.6 µmol m^{-3}), a low nutrient concentration(16.80±0.48 µmol m^{-3} for NO_3, 1.10±0.05 µmol m^{-3} for PO_4) and a very high salinity (35.083±0.019) (Talley et al., 2011).

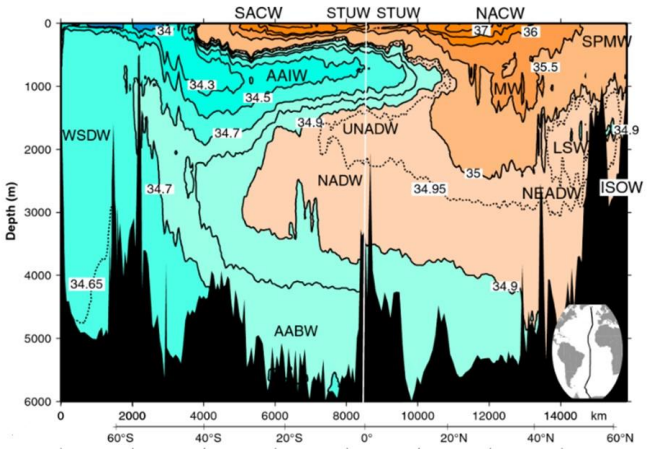

Figure 8 Water masses in the Atlantic Ocean, the numbers stand for the salinity (Tulley et al., 2011)

Antarctic Bottom Water (AABW) flows below 4000m and is formed south of the ACC in the Wendell Sea through mixing of the Circumpolar Deep Water (CDW) and the Wendell Sea bottom water (WSBW) and has a density of γ > 28.20 kg m-3 (Liu and Tanhua, 2021). The relatively warm CDW arrives from the north with the ACC and mixes with the very cold WSBW arriving from the south (Liu and Tanhua, 2021). AABW can be described by very high salinity (34.830±0.009), high silicate content (124.87±2.36 µmol m^{-3}) and low temperatures (-0.46±0.24 °C) (Liu and Tanhua, 2021). AABW joins the ACC and flows into the Cape basin from the south, close to the African continent the water is diffracted and part of it returns towards the Agulhas region (Saunders et al., 1995). After crossing the ACC the AABW exchanges water with the NADW.

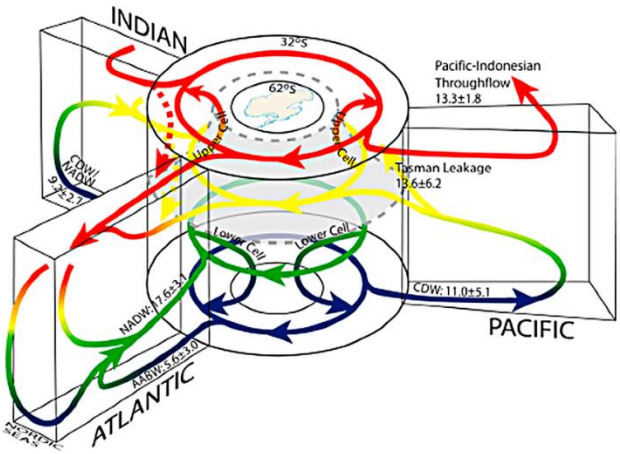

Figure 9: Global overturning circulation, numbers showing the transported volume by each water mass (Meredith et al., 2011)

2.6 Anthropogenic carbon in the Atlantic Ocean

Deep water formed in the North Atlantic Ocean mainly stays within the Atlantic basin, thereby forming a confined reservoir for anthropogenic carbon. This basin has been thoroughly investigated and Gruber et al. (2019) showed it was the biggest anthropogenic carbon reservoir on earth in the period 1994-2007. The reservoir owes its large anthropogenic carbon storage capacity to the deep water formation in the North Atlantic.

The upper overturning cell in the South Atlantic, creating the AAIW, takes up a lot of anthropogenic carbon which is stored between 30°S and 50°S, this is the second deepest anthropogenic carbon reservoir on earth (Gruber et al., 2019). Anthropogenic carbon is taken up at the surface and transported along sloping Isoneutral surfaces into the internal ocean. Investigating the C_{ant} distribution along these surfaces is therefore informative.

For both the AAIW and the AABW part of the newly formed water is transported into the Indian ocean (Stramma and England, 1999). The potential anthropogenic carbon it contains is therefore distributed over a larger area than in the North Atlantic, but it has been less investigated. Müller et al. (2023) found a shift in the main anthropogenic carbon storage reservoir in the Atlantic Ocean from the North, to the South Atlantic in the period from 1994 to 2014. This is another reason why the transect at 40°S is an interesting sight to study.

3. Methods and methodology

3.1 C* calculation

The Global Ocean Data Analysis Project version 2 (GLODAPv2.2022) was used to obtain the data on the transect. The cruises that had datapoints between 38°S and 42°S and that had data for all the different components needed to calculate the anthropogenic carbon concentration were selected. Further quality control was done by Louise Delaigue. To calculate C_{ant} concentration the C* method was used, this method is based on the fact that changes in the DIC concentration are caused by a combination of natural and anthropogenic processes (Gruber et al., 1996). The anthropogenic

fraction of the total DIC is outweighed by the natural DIC fraction, this is why it is important to eliminate this natural fraction:

$$C_{ant} = DIC_{measured} - DIC_{bio} - DIC_{phys} \quad \text{(Eq. 15)}$$

The fraction of the DIC that is added by the carbonate pump is removed first:

$$C^* = DIC_{measured} - \delta\frac{C}{-AOU} \cdot AOU - 0.5 \cdot TA \quad \text{(Eq. 16}_A\text{)}$$

$$C^* = DIC_{measured} - \delta\frac{C}{PO4} \cdot PO_4 - 0.5 \cdot TA \quad \text{(Eq16}_B\text{)}$$

$$C^* = DIC_{measured} - \delta\frac{C}{NO3} \cdot NO_3 - 0.5 \cdot TA \quad \text{(Eq16}_C\text{)}$$

In theory, all these methods should give the same C* value. I decided to continue with the C* values where nitrate and AOU were used in the calculations to minimize the error in the C*. Phosphate was excluded because of its lower concentration in the ocean (Eq. 13), that resulted in a bigger error window for the C* than when nitrate or AOU was used.

Equation 17 for C* is not complete because the DIC and TA are not only affected by the carbonate pump but also by the soft tissue pump. As organic matter is degraded nutrients are released into the water column (Eq. 11/ 13), decreasing TA. The complete equation for C* is then, using the nitrate unit (Eq. 8):

$$C^* = DIC_{measured} - \delta\frac{C}{-AOU} \cdot AOU - 0.5 \cdot (TA + 1.36 \cdot NO_3) \quad \text{(Eq. 17}_A\text{)}$$

$$C^* = DIC_{measured} - \delta\frac{C}{NO3} \cdot NO_3 - 0.5 \cdot (TA + 1.36 \cdot NO_3) \quad \text{(Eq. 17}_B\text{)}$$

The C* value reflects the natural and anthropogenic CO_2 exchange through the air-sea interface and should stay about constant with depth, as the increase due to biology has been corrected for (Gruber et al., 2019). In this calculation a surface concentration of zero for AOU and nitrate is expected, this is however not the case as can be seen in figure 10.

To correct for this the surface water concentrations where the water masses are formed are subtracted from the concentration measured at depth:

$$C^* = DIC_{measured} - \delta\frac{C}{NO3} \cdot (NO_{3\ depth} - NO_{3\ surface}) - 0.5 \cdot (TA + 1.36 \cdot NO_3) \quad \text{(Eq. 18}_A\text{)}$$

$$C^* = DIC_{measured} - \delta\frac{C}{-AOU} \cdot (AOU_{depth} - AOU_{surface}) - 0.5 \cdot (TA + 1.36 \cdot NO_3) \quad \text{(Eq. 18}_B\text{)}$$

The formation regions of the water masses found at the transect at 40°S are shown in figure 10, the conditions from which these regions are selected were made by Lui and Tanhua (2021). For NADW the upper NADW formation region was used to calculate the initial conditions.

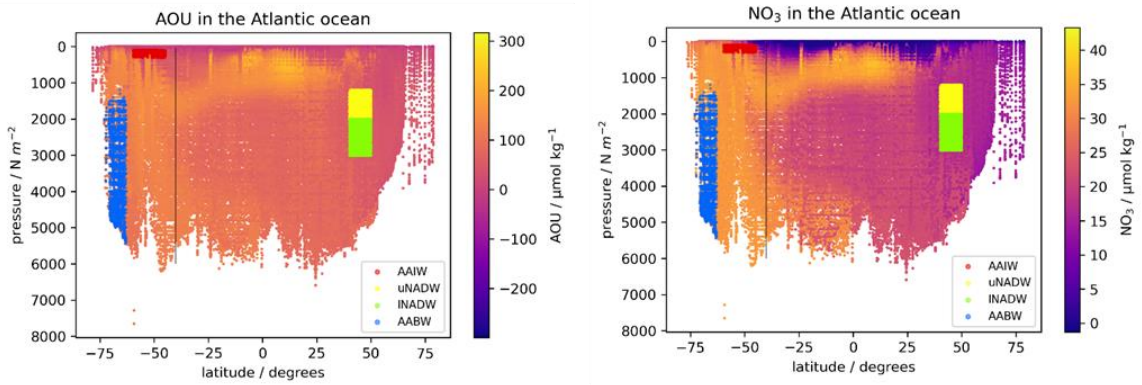

Figure 10: AOU and NO_3 concentrations in the Atlantic Ocean. The Location of the transect is pointed out with the black line. The colored regions are the locations of water mass formations of the different water masses, according to Liu and Tanhua (2021)

3.2 eMLR method to calculate C*

In order to calculate the C_{ant} concentration using coefficient values, the C* is calculated again but now the MLR method is applied that generates coefficient values. An eMLR is a statistical approach to to find the relative importance of several (independent) coefficients based on fitting lines through the datapoints. With those independent coefficients the dependent variable, C* in this case, is calculated. The relationship between the independent coefficients is used to calculate the C* in the end, by multiplying the coefficient with their corresponding variable:

$$C^*(t_1) = a_1 + b_1 \cdot T_1(t_1) + b_1 \cdot T_1^2(t_1) + c_1 \cdot T_2(t_1) + c_1 \cdot T_2^2(t_1) \ldots + z_1 \cdot T_k(t_1) \qquad \text{(Eq. } 19_A\text{)}$$

$$C^*(t_2) = a_2 + b_2 \cdot T_1(t_2) + b_1 \cdot T_1^2(t_2) + c_1 \cdot T_2(t_2) + c_1 \cdot T_2^2(t_2) \ldots + z_1 \cdot T_k(t_2) \qquad \text{(Eq. } 19_B\text{)}$$

The possible coefficients used in this study are temperature, salinity, nitrate, silicic acid, oxygen and AOU. How many and which coefficients are used depends on the fit. A probalistic approach is used to find out which coefficients will be used, according to Gruber et al. (2019). A minimum of 2 and a maximum of 5 coefficients were used, which led to a total of 56 combinations. Out of these combinations the 10 runs with the slope values closest to 1 were selected and mean value for each coefficient is calculated. With those mean values the C_{ant} is calculated, making use of the climatological value of each variable.

Following Friis et al. (2005) the coefficients of the two C* values that are seperated in time are subtracted from each other. This way the measurement errors that are included in both C* calculations are partly canceled out (Sabine 2010). The combined coefficients form an estimate of the anthropogenic carbon:

$$\Delta C_{ant}(t_2 - t_1) = (a_2 - a_1) + (b_2 - b_1) \cdot T_{clim1} + (b_2 - b_1) \cdot T_{clim1}^2 + (c_2 - c_1) \cdot T_{clim2} + \ldots (z_2 - z_1) \cdot T_{climk} \quad \text{(Eq. 20)}$$

In equation 20 the climatological distributions of the predictors are used rather than using values from the most recent year, to avoid seasonality.

A Monte Carlo analysis was applied to the eMLR to calculate the standard deviation in the C_{ant} created by the uncertainties in the variables. The uncertainties by GLODAP are given in table 1 and the standard deviation was calculated over 1000 iterations over the eMLR (Lauvset et al., 2022).

Later in the calculations to be able to subtract the values from one year from the values from another it was necessary that the amount of datapoints are the same. To make sure this is the case datapoints were interpolated over the amount of datapoints from the most recent year.

Variable	Minimum adjustment
Salinity	0.005
Oxygen	1%
Nutrients	2%
DIC	4 µmol kg^{-1}
TA	4 µmol kg^{-1}
pH	0.01

Table 1: Minimum bias relative to the measurement precision and the different cruises included. These numbers are not uncertainties but they can be seen as inter-cruise consistency in the data product (After Lauvset et al., 2022, table 3).

3.3 Definition of the water masses

The eMLR calculates the C_{ant} for each water mass, the water masses are separated on neutral density levels that are shown in table 2. Because the neutral density levels in the surface waters vary a lot with depth and location, the AAIW and SACW shows a lot of overlap. That is why I decided to merge the SACW and the AAIW into one water mass in the calculations.

Water mass	gamma
SACW/ AAIW	24.00< ϒ <27.55
NADW	27.55< ϒ <28.10
AABW	ϒ > 28.10

Table 2: Separation of the different water masses based on neutral density levels

4. Results

4.1 Nutrient distributions

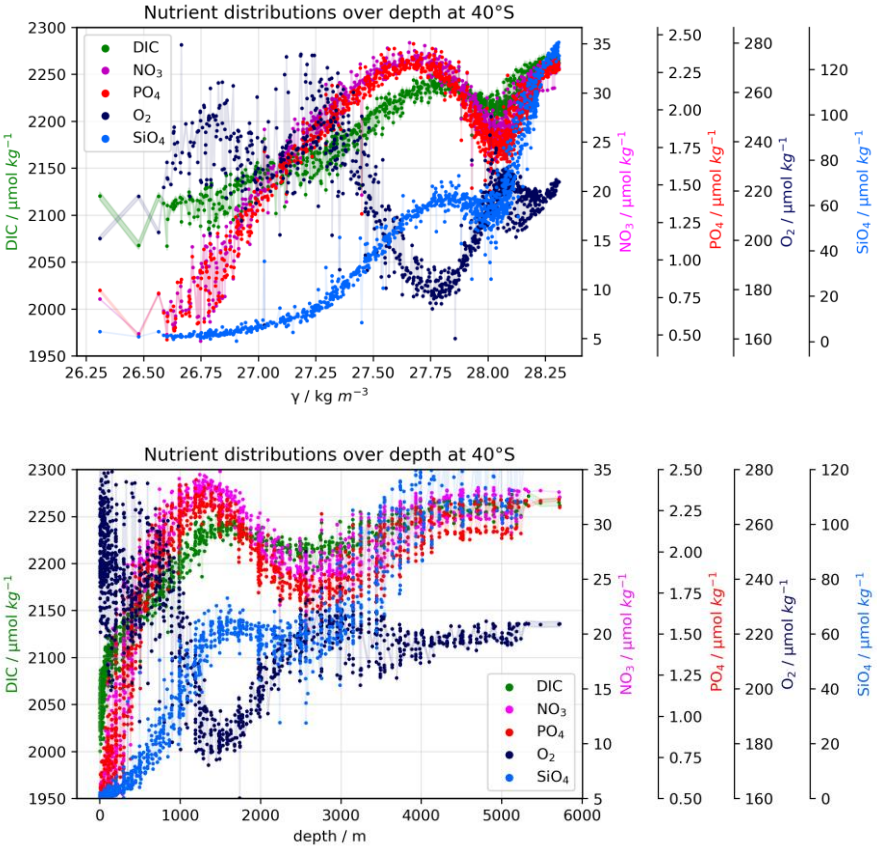

Figure 11: Nutrient distributions at 40°S against depth and neutral density

Figure 11 shows that the ratios of the different nutrients are not constant over depth at the transect. This can be related to the stratification of the different water masses that are present at the transect. The DIC concentration for example, is expected to increase with increasing depth because remineralization adds DIC to the water column. But at a certain neutral density level the DIC starts to decrease, this is at the transition of AAIW to NADW, after the transition from NADW to AABW the concentration increases again. The same trend is visible for the nutrients that are plotted, and oxygen shows an opposite trend which is typical for NADW (Talley et al., 2011, Giresse et al., 2007). The silicate concentration is much higher in the AABW than in the rest of the water column, this is because the silicate concentration is very high in the circumpolar deep water, where the AABW is formed (Tréguer 2014).

For the purpose of this transect study at 40°S all the points across the various longitudes are grouped together because the nutrient concentrations are constant along the latitude. An example of this is shown in figure 12 where all the nitrate concentrations of cruise 4095 are plotted against depth. Cruise 4095 sailed across the whole transect (Figure 2, 2012) and the nitrate concentrations stayed constant along the transect. In the eMLR all the points in one year are therefore grouped together as one. The eMLR is then run for every year with datapoints on the transect.

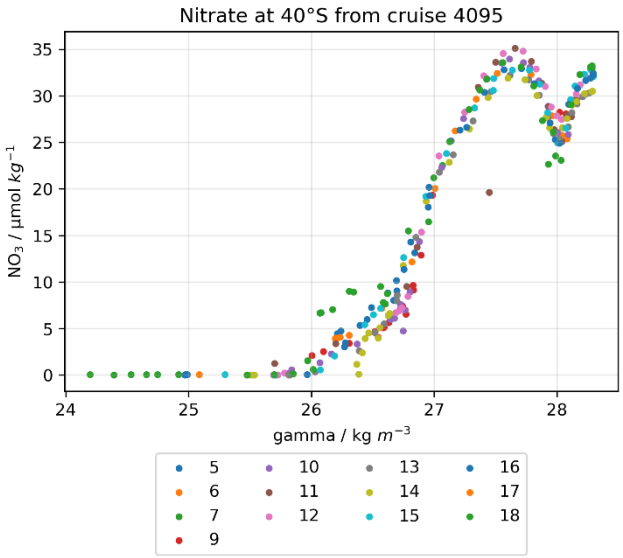

Figure12: Constant nitrate distribution along the whole transect

4.2 Different carbonate species

Figure 13 shows the distribution of the different carbonate species over depth, where the bicarbonate ion is the most dominant, followed by the carbonate ion and CO_2(aq), as expected. The carbonate ion is high in the surface and decreases with depth, this decrease can be related to the decreasing temperature and increasing pressure with depth, resulting in an increase in p*K* values (Equation 4 and 5) and a decrease in the carbonate ion concentration (Zeebe et al., 2002). This drop in carbonate ion concentration is intensified by the results of the biological pump. In the surface waters CO_3^{2-} is used to form $CaCO_3$ shells, decreasing the concentration, while the concentration is increased by the production of organic matter. The impact of this second process can be up to 5 times higher, leading to a high CO_3^{2-} concentration in the waters that where light can reach and photosynthesis is happening (Sarmiento and Gruber, 2006). When these organisms die they sink deeper into the water column and are eventually decomposed (Blank and Gruber, 2007). During remineralization CO_2 is released, most of which is transformed into HCO_3^-, leading to an opposite trend with respect to the carbonate ion. The water masses in the South Atlantic are stratified and the NADW carries a low DIC concentration which results in a dip in the plot. The same trajectory is continued in the AABW.

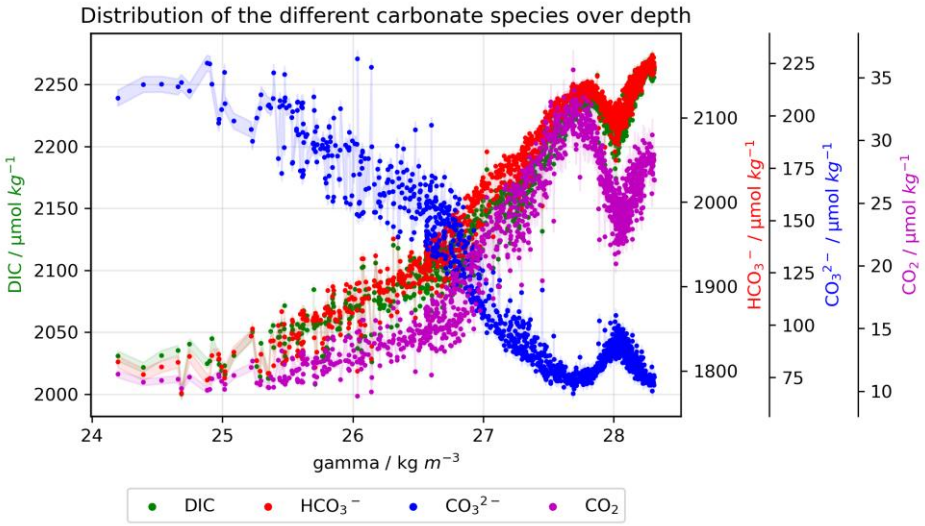

Figure 13: The distribution of the different carbonate species over depth

4.3 C* calculation

Figure 14 shows how the C* values change over depth, calculated using AOU, PO_4 and NO_3 (Equation 18). The C^*_{NO3} and the C^*_{PO4} values are lower than the C^*_{AOU} value at depth. This is because the surface concentrations of nitrate (and phosphate) are higher than those for AOU (Figure 10) and thus the assumption that the surface concentrations were zero is further off for nitrate and phosphate.

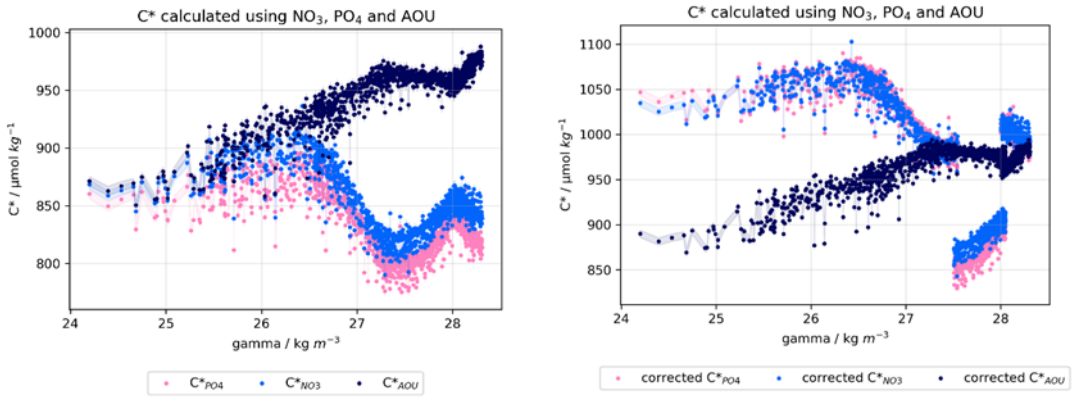

Figure 14: The left plot shows the C distribution over depth calculated with nitrate, phosphate and AOU all the data points from all the years were included in this plot. The figure on the right shows the same but corrected for the concentrations at the location of water mass formation*

The values at depth were corrected for the surface concentrations by subtracting the concentration of that variable at the location of water mass formation (Equation 18). After the corrections all three C* values are closer together in the main part of the water column (Figure 14B). The surface concentrations of NO_3 and PO_4 were less high in the formation region of the NADW, leading to a less pronounced correction. This can be seen in figure 14, between neutral density levels 27.55< ϒ <28.10. The C^*_{AOU} is changed the least after the correction but it still gives the most constant value over depth, this is why it is used for later calculations. A more constant value over depth is convenient in the eMLR calculations of C*, as less variance will need to be explained in the model. This will lead to smaller root-mean-square errors (RMSE) of the model.

An example of the C* produced by the eMLR is plotted against the C* that is calculated is shown in figure 15. Such a figure was made for every water mass, every cruise and every set of coefficients (3*8*56= 1344 plots). For every cruise, the 10 sets of coefficients that resulted in the slope values closest to 1 were selected and the C_{ant} values were calculated with a mean of those 10 values (Equation 19).

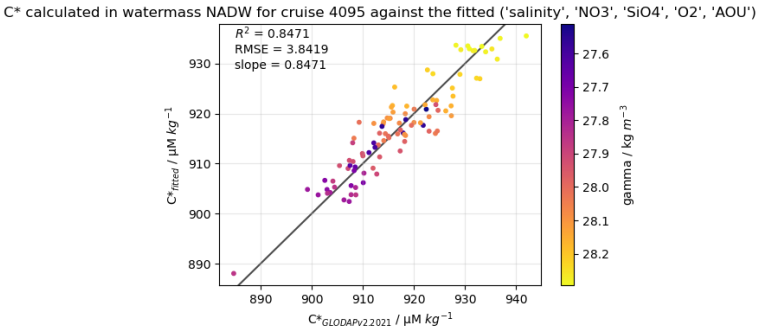

Figure 15: C calculated plotted against the C* value produced by the eMLR*

The Redfield Ratio shown in equation 14 may not always be constant everywhere. Deeper in the water column the nutrient concentrations may change with different water masses. Figure 16 shows the nutrient ratios in the Atlantic Ocean, these plots include all the datapoints in the Atlantic Ocean available in GLODAP(1972-2020). However the trends in nutrients are still visible; mainly the N:P ratio follows the expected trend. The surface ocean contains more carbon than expected from the Redfield Ratio (Equation 13). This may be correlated to processes that affect the DIC but not the nutrient concentrations, like the C_{ant} penetration in the surface ocean.

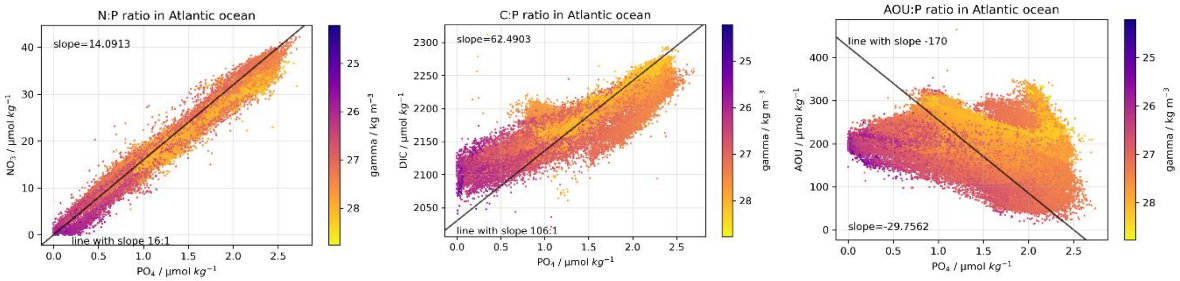

Figure 16: Redfield ratios in the Atlantic Ocean. The black line plotted through the datapoints is the 'expected' Redfield ratio

On the transect the nutrient ratios are not constant with depth, resulting in non-constant Redfield Ratios with depth (Figure 17). This can again be related to the stratified ocean at this transect, with each water mass having a different nutrient composition.

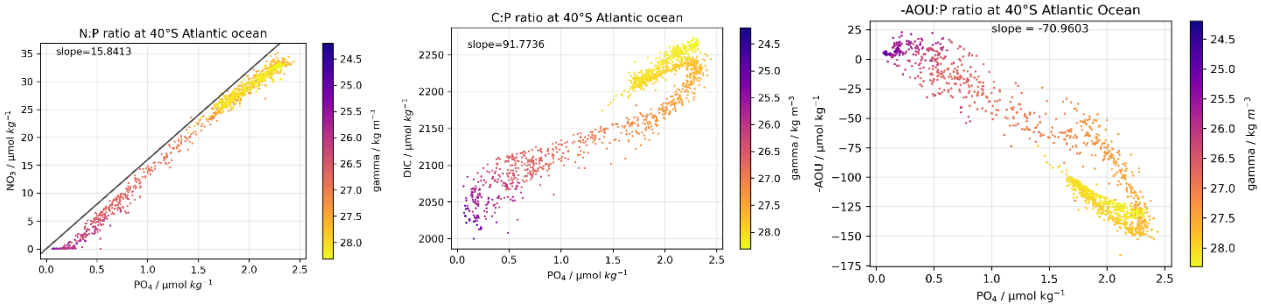

Figure 17: Nutrient ratios over depth at the transect at 40°S

In this study constant Redfield Ratios were used during the C* calculations, but it might be more accurate to use Redfield Ratios that change with neutral density levels. In the surface waters the increased DIC concentration is visible and the C:P and AOU:P trends have a different slope in the deep ocean than in the surface.

4.4 Anthropogenic carbon

As expected from C_{ant} that enters the ocean through the air-sea interface, the concentration is highest in the surface and decreases rapidly with depth (Figure 18). At the edge of the water masses between AAIW and the NADW a very steep increase is visible. This can be related to the difference in ranges of the climatological variables and the values of the variables in the GLODAP database. In the eMLR each variable is used twice: once multiplied with its corresponding coefficient, and once squared and multiplied with its coefficient. Here it is important that the range of the climatological values is equal to the range in GLODAP values because the value that is inserted will be squared and a small deviation can suddenly become very big.

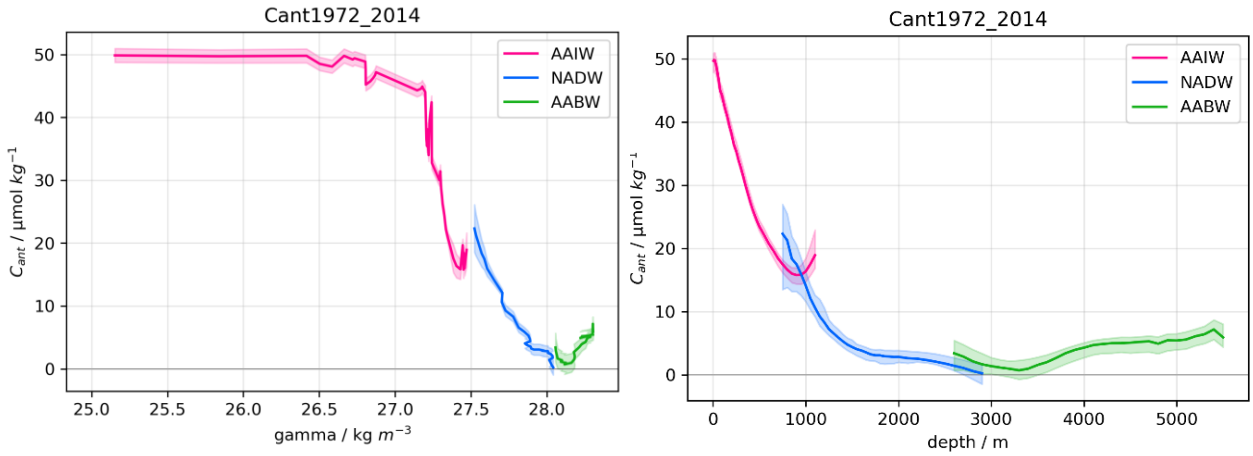

Figure 18: The Anthropogenic carbon concentration against depth and neutral density plotted for the period 1972-2014

The coefficient value is set while using the GLODAP dataset and if the range in climatological values is bigger than the range in GLODAP values the squared value of the climatological values can fall on the steeply sloping part of the squared curve, forming the parabola out of the squared function.

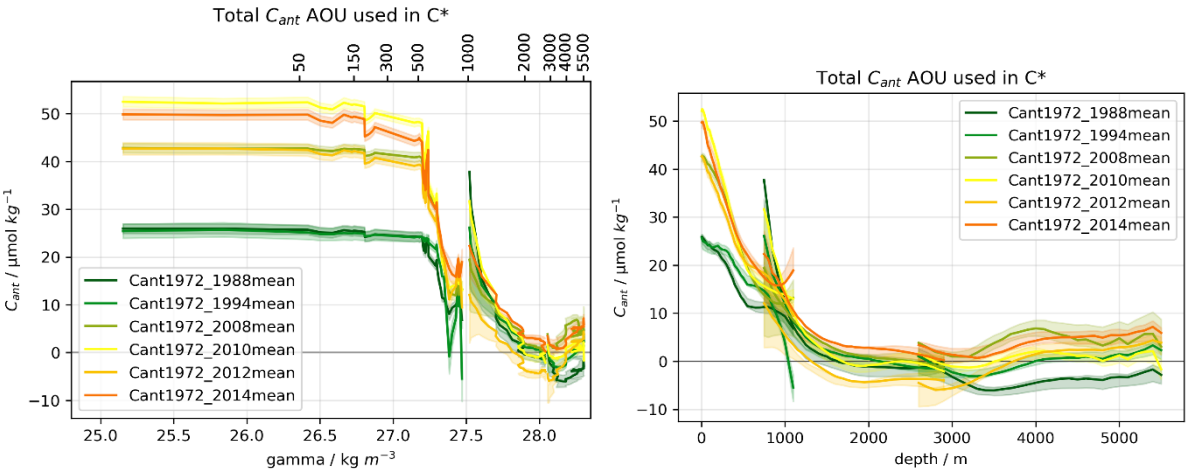

*Figure 19: Total inventory increase over time plotted against neutral density, C_{ant} is calculated using AOU in the calculations for C**

Figure 19 shows the total increase in inventory over time. The biggest increase is visible in the upper 1000m and the C_{ant} penetration depth has increased over time. The C_{ant} concentration decreases rapidly with depth after that, table 3 shows the concentrations in each water mass per square meter.

This table also shows the increase of C_{ant} over time, with a clear jump between 1994 and 2008, and some smaller increases and decreases between 2008 and 2014.

Water mass	**1972-1988**	**1972- 1994**	**1972- 2008**	**1972- 2010**	**1972- 2012**	**1972- 2014**
AAIW / mol m^{-2}	14.1 ± 0.798	16.5 ± 0.903	22.5 ± 0.832	24.5 ± 0.808	22.5 ± 0.810	24.4 ± 0.791
NADW / mol m^{-2}	4.65 ± 2.52	6.39 ± 2.46	7.16 ± 2.25	6.56 ± 2.20	-2.53 ± 2.24	10.5 ± 2.40
AABW / mol m^{-2}	-10.1 ± 3.26	-1.73 ± 2.71	9.72 ± 3.26	1.29 ± 3.53	-1.04 ± 3.16	8.12 ± 2.73
SUM / mol m^{-2}	8.70 ± 6.57	21.2 ± 6.07	39.4 ± 6.34	32.3 ± 6.54	19.0 ± 6.20	43.0 ± 5.92
SUM <3000m / mol m^{-2}	18.8 ± 3.31	22.9 ± 3.36	29.6 ± 3.08	31.0 ± 3.01	20.0 ± 3.05	34.9 ± 3.19

Table 3: Column inventories per m^2 on the transect, AOU is used in the calculations for C.*

A second eMLR was made, using nitrate to calculate the C* instead of AOU (Equation 18), in order to get rid of the apparent increase in C_{ant} in the AABW. Figure 20 shows that the apparent increase is gone but that the overall carbon concentration in the bottom water is higher and it increases with time. The anthropogenic carbon concentration in the surface water is higher than for $C_{ant\text{-}AOU}$ and the transition from AAIW to NADW is much less smooth. The C_{ant} concentration decreases to zero at a shallower depth than for $C_{ant\text{-}AOU}$, except for the last year. The surface water does not contain the highest concentration in $C_{ant\text{-}NO3}$, for all years except for the last the concentration first increases before it decreases with depth. For both methods the C_{ant} concentration in the most shallow part of the AAIW is much higher in the first time period than the rest of the years.

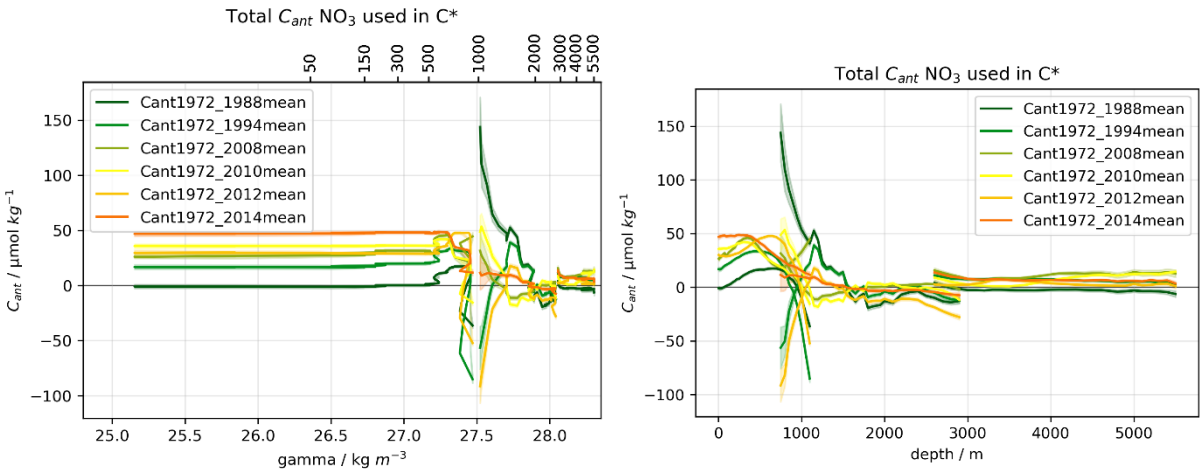

*Figure 20: Total inventory increase over time plotted against neutral density, C_{ant} is calculated using NO_3 in the calculations for C**

Table 4 shows the column inventories per m^2 for the transect and for the inventories above 3000m, both methods fall within the error ranges for most years.

Water mass	**1972-1988**	**1972- 1994**	**1972- 2008**	**1972- 2010**	**1972- 2012**	**1972- 2014**
AAIW / mol m^{-2}	9.89 ± 1.08	22.4 ± 0.863	27.6 ± 1.04	27.0 ± 0.961	33.0 ± 1.08	34.2 ± 1.01
NADW / mol m^{-2}	16.8 ± 2.72	5.75 ± 3.57	-1.35 ± 2.74	1.92 ± 2.42	-16.6 ± 2.24	1.69 ± 2.69
AABW / mol m^{-2}	-6.31 ± 3.73	16.7 ± 2.49	25.3 ± 3.80	14.7 ± 1.81	8.55 ± 2.52	16.4 ± 2.37
SUM / mol m^{-2}	20.4 ± 7.53	44.8 ± 6.92	51.5 ± 7.58	43.6 ± 5.19	25.0 ± 6.51	52.3 ± 6.08
SUM <3000m / mol m^{-2}	26.7 ± 3.80	28.2 ± 4.43	26.2 ± 3.79	28.9 ± 3.38	16.5 ± 3.99	35.9 ± 3.71

Table 4: Column inventories per m2 on the transect, NO_3 is use in the calculations for C.*

5. Discussion

5.1 Explaining the C_{ant} distribution over depth

The steep increases at the transition from the AAIW to the NADW (visible in figures 18, 19 and 20) can be related to the difference in ranges of the climatological variables and the values of the variables in the GLODAP database. In figure 21 each variable is plotted against its climatological variant. For AOU, nitrate, silicate and salinity the climatological values are consistently higher in the surface than the concentrations reported in GLODAP. The range for oxygen and salinity is higher in a deeper part of the water column. This may explain the steep deviation from the curve in figures 18, 19 and 20.

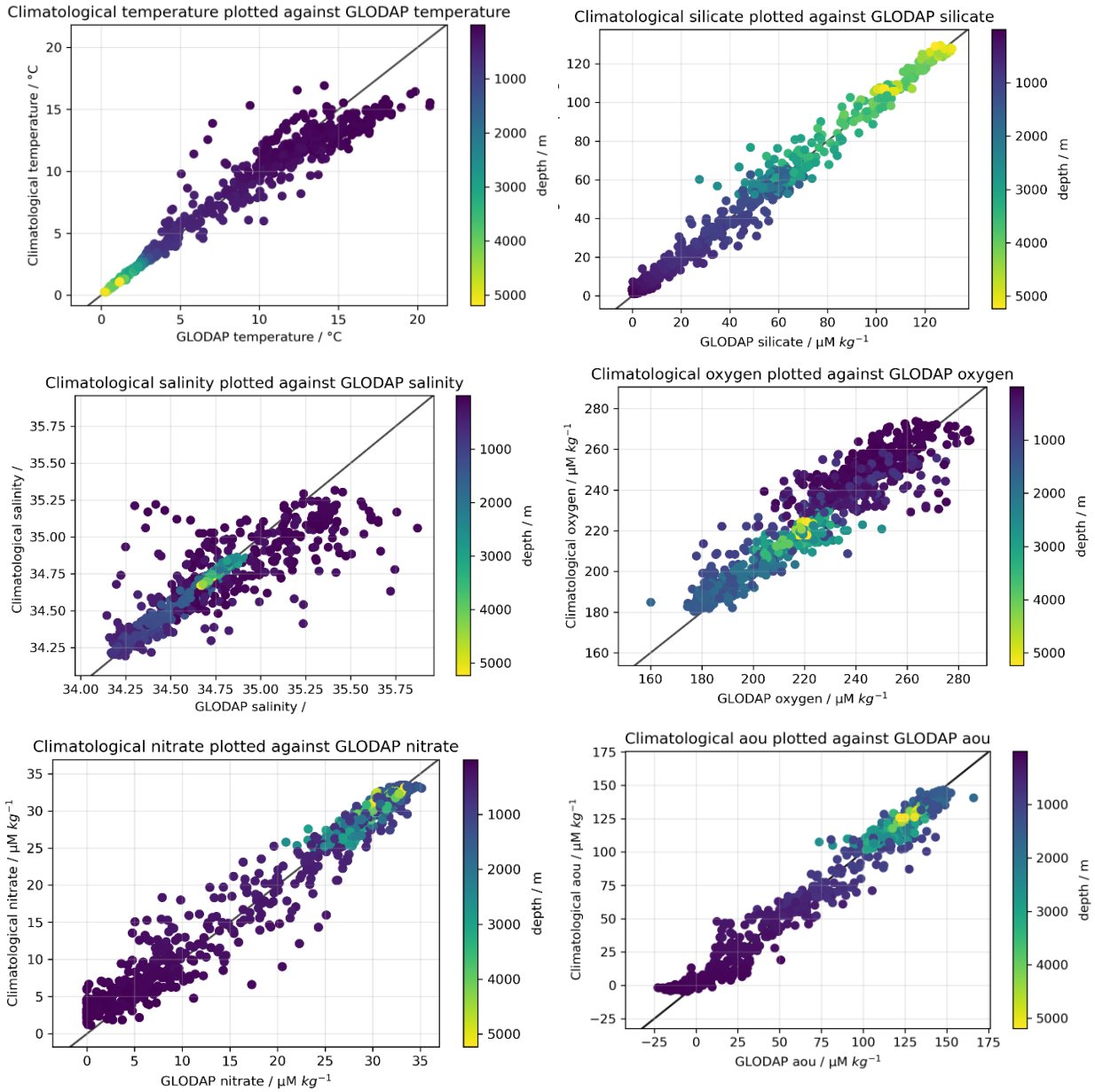

Figure 21: Each variable is plotted against its climatological variant. A 1:1 line is plotted so a deviation from this line can be easily spotted

5.2 Comparing $C_{ant\text{-}AOU}$ to $C_{ant\text{-}NO3}$

The plots in figures 19 and 20 show similar trends; a constant concentration in the surface waters followed by a rapid decrease in C_{ant} around 27.5 kg m^{-3}. The values per m^2 (tables 3 and 4) are similar enough to fall within the error ranges for most years, between $C_{ant\text{-}AOU}$ and $C_{ant\text{-}NO3}$. Figure 19 shows an apparent increase of $C_{ant\text{-}AOU}$ in the AABW, this increase can be related to the increase in nitrate, phosphate and DIC while the oxygen concentration stayed about constant (Figure 11, more visible in the plot against depth). This could have caused the eMLR to falsely interpret the signal as an anthropogenic carbon signal. The $C_{ant\text{-}NO3}$ signal does not increase again with depth.

Where the $C_{ant\text{-}AOU}$ concentration is highest at the surface and decreases with depth, the concentration increases slightly in the subsurface for $C_{ant\text{-}NO3}$, except for the last year. A reason for this could be the causes of uncertainty that have not been accounted for in the analysis. The error ranges provided by the GLODAP database were accounted for (table 1), however, inter-cruise uncertainties were not. Mainly for the $C_{ant\text{-}NO3}$ the error range is very narrow, which most likely means that there is a source of uncertainty missing.

The seasonal differences between the cruises could also have a big impact on the surface water CO_2 concentration. The cruise in 1972 happened in December, and most other cruises were also done during Austral summer. Except for the cruise in 2010, that happened in October just before or during the time of the year when spring bloom is happening, resulting in a lower or higher DIC concentration, respectively. While the cruises in 2008, 2012 and 2014 happened later in the summer (in January and February) which resulted in higher DIC concentrations, possibly misleading the eMLR. The deviating Redfield Ratios with depth at the location of the transect (Figure 17) might also lead to fluctuations in the C_{ant} concentration.

The $C_{ant\text{-}NO3}$ concentration decreases more rapidly with depth than $C_{ant\text{-}AOU}$, except for the last year. The $C_{ant\text{-}NO3}$ concentration has already dropped to zero in the AAIW, while this only happened in the NADW for $C_{ant\text{-}AOU}$. AAIW carries by far the highest C_{ant} concentration in both $C_{ant\text{-}NO3}$ and $C_{ant\text{-}AOU}$. AAIW is in these calculations a combination of SACW and AAIW, where SACW mainly makes up the upper part of this water mass and AAIW the lower part. The SACW is ventilated on timescales of less than a decade, which results in efficient transport of C_{ant} into the ocean interior (Gruber et al., 2019). Both C_{ant} plots show this homogenously spread C_{ant} concentration in the surface waters, $C_{ant\text{-}AOU}$ more than $C_{ant\text{-}NO3}$.

The AAIW is formed between 40° and 55°S and from there spreads northwards into the Atlantic basin (Liu and Tanhua, 2021). AAIW is formed out of surface water in the ACC, the C_{ant} is high in the water mass because surface waters are often well-ventilated. In the AAIW the deepest waters were formed out of the densest and deepest part of the ACC water, which contains a lower concentration of C_{ant} than ACC surface waters. This leads to a decrease of C_{ant} with depth. The C_{ant} penetration will eventually reach neutral density layers with higher densities and the rapid decrease of C_{ant} will flatten out. This process has already started since the depth at which the steep decrease starts is deeper than at the start. Moreover, the C_{ant} concentration below the thermocline will increase, at this depth the solubility is higher, meaning that more C_{ant} can be stored here. Mixing by diffusion plays an important role in transporting C_{ant} vertically in the Atlantic Ocean. In regions where strong gradients in C_{ant} are present, between upper and deep layers, diffusion is the main process of transporting C_{ant} into the deep ocean (Caínzos et al., 2022).

In the North Atlantic Ocean the formation of NADW leads to the deepest penetration of C_{ant} in the ocean. These high density waters with elevated C_{ant} levels are restricted to areas close to the deep water formation. This, in combination with surface waters that are ventilated on a timescale of

several decades, leads to the highest inventory increase in the period from 1994 to 2007 (Gruber et al., 2019, Clement et al., 2018). The rapidly southward flowing NADW brings these waters with elevated C_{ant} concentrations into the southern hemisphere. The North Pacific ocean is lacking deep water formation, that is why C_{ant} is restricted to the surface ocean here. These differences in location and the presence (or lack) of deep water formation in that region leads to large differences in C_{ant} penetration depth around the globe. Figures 19 and 20 show that part of the C_{ant} in the NADW has already been transported into the southern hemisphere, as the concentration of C_{ant} is positive in the most recent years.

5.3 Comparison to other findings

In the studies of Gruber et al. (2019) and Clement et al. (2018) the C_{ant} concentration in the ocean was calculated for a period from 1994 to 2007, as they wanted to estimate decadal changes between the 1990s and the 2000s. Figure 3A out of Gruber et al. (2019) shows that around 16 moles of C_{ant} per m^2 were taken up by the ocean around 40°S. Gruber et al. (2019) calculated the C_{ant} concentration up until 3000m dept and an additional 0.3 mol was added for the deeper parts of the water column.

Table 5: column inventories for the period 1994-2008

Table 5 shows the column inventories calculated at the location of the transect for the same time period as was used in Gruber et al. (2019). The sum <3000m for $C_{ant\text{-}AOU}$ is lower than expected. Adding the extra 0.3 moles for the rest of the water column, the ~16 moles by Gruber et al. (2019) falls just outside of the error range. The sum <3000m for $C_{ant\text{-}NO3}$ is much higher than expected, mainly because the AAW value could be an overestimation.

water mass	**$C_{ant\text{-}AOU}$ 1994-2008**	**$C_{ant\text{-}NO3}$ 1994-2008**
AAIW / mol m^{-2}	8.59 ± 1.34	24.43 ± 1.55
NADW / mol m^{-2}	0.529± 4.10	6.32± 5.36
AABW / mol m^{-2}	13.22± 4.51	14.24± 5.14
SUM / mol m^{-2}	22.34± 9.95	44.99±12.05
SUM < 3000m / mol m^{-2}	9.12± 5.44	30.75± 6.91

Table 6 shows the C_{ant} transport at 30°S in the upper and lower layer of the Atlantic Ocean (and the net sum) that was found by Caínzos et al. (2022). Positive values mean a transport from south to north, and vice versa. The net transport is northwards and it increases with time, with a big jump from the second to the third period. This is the result of an increase in the strength in circulation which led to more C_{ant} transport. The southward transport also increased. The C_{ant} concentration in the NADW decreases with an increase in distance from the source; further south. This table shows that the NADW carries a bit of C_{ant} southwards, and thus it is likely that the NADW at 40°S also still carries some C_{ant}. The C_{ant} concentration in the NADW at 40°S will increase over time, as the southward transport increases (Caínzos et al., 2022).

	1990-1999 Pg C yr^{-1}	**2000-2009 Pg C yr^{-1}**	**2010-2019 Pg C yr^{-1}**
Upper	0.208± 0.015	0.252± 0.016	0.404± 0.023
Lower	-0.033± 0.012	-0.055± 0.011	-0.070 ± 0.012
sum	0.175± 0.019	0.197± 0.019	0.334± 0.026

Table 6: C_{ant} budget in the South Atlantic Ocean at 30°S by Caínzos et al. (2022)

5.4 Carbonate system through time

5.4.1 ΔC_{ant} and ΔDIC

Figure 22 shows the surface water increase of the DIC concentration over the years. The DIC concentration in the surface only increased with time while the concentration in the deep water stayed about constant.

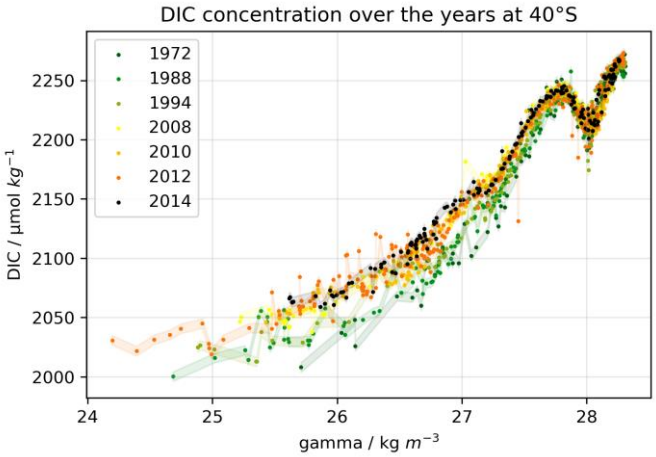

Figure 22: The increasing DIC concentration over the years

To see how much of the increase in DIC in the surface waters can be related to the C_{ant} increase, $C_{ant\text{-}AOU}$ and $C_{ant\text{-}NO3}$ were added to the 'original' DIC values from 1972 (Figure 23). This is done by interpolating the C_{ant} data to match the DIC data.

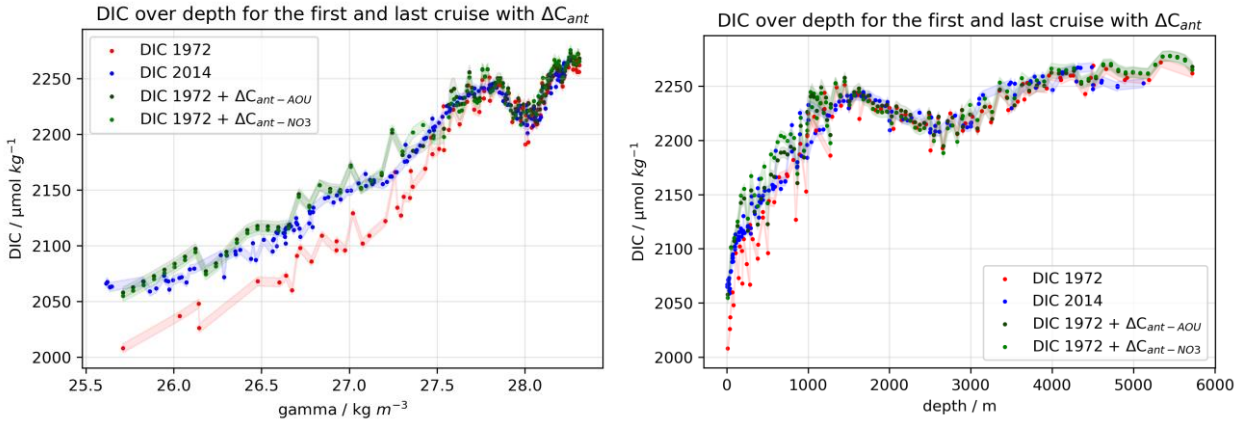

Figure 23: The DIC concentration in the first and last year against neutral density and depth. The C_{ant} increase over the period 1972-2014 was added to the DIC concentration of the first year.

Figure 23 shows that the increase in DIC in the period 1972-2014 is very similar to the increase in C_{ant} over that same period meaning that most of this increase in DIC can be attributed to the increase in C_{ant}.

In order to see where in the water column the biggest change in DIC concentration occurred, the DIC values from the first cruise (1972) were subtracted from the DIC values of the last cruise (2014) (figure 24). The biggest difference in DIC is found around 27 kg/ m^3, deeper than ~28 kg/ m^3 the DIC concentration mainly decreased.

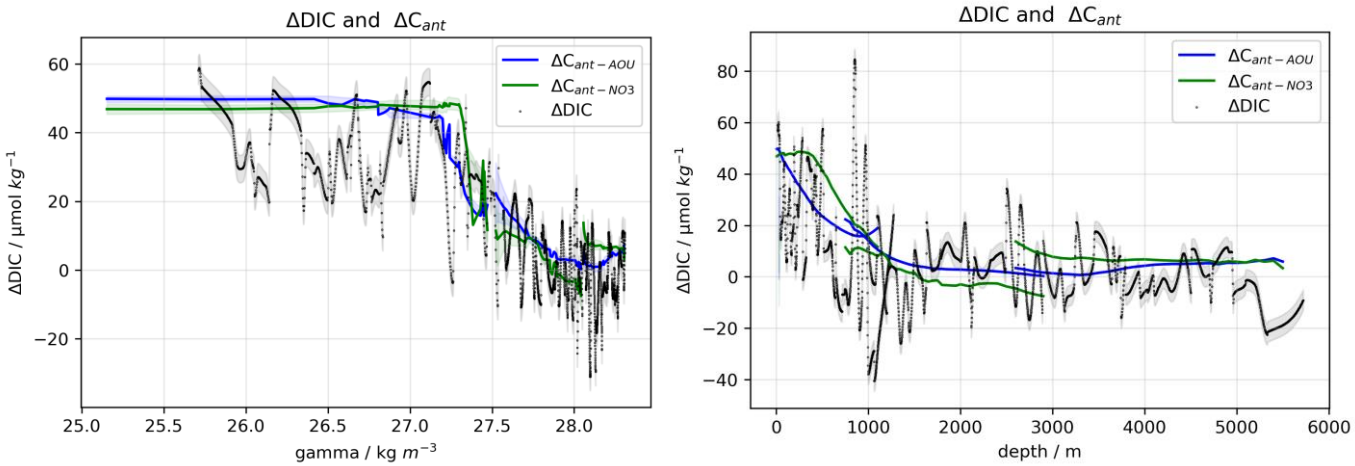

Figure 24: The DIC concentration from the first year were subtracted from the DIC concentrations in the last year and plotted against depth and neutral density. The C_{ant} increase over this same period was plotted on top of it.

Next to the difference in DIC the C_{ant} increase is also plotted in figure 24 and both lines definitely follow the same trend but the DIC plot has more variation than the C_{ant} plots. This is because DIC is also affected by other processes, e.g. the biological pump, and not just by the C_{ant} concentration. The addition of C_{ant} happens next to the natural processes and therefore the fluctuations in the ΔDIC plot are likely not anthropogenic carbon related. Remineralization of organic matter is the most efficient way of increasing the DIC concentration at depth. At the depth range where active remineralization is happening, the ΔDIC line still mainly follows the C_{ant} concentration, with some depths where the ΔDIC deviates.

Figure 24 shows that there are no processes adding to the DIC concentration significantly other than the increasing C_{ant} concentration. This proves that almost 100% of the increase in DIC can be ascribed to the increase in C_{ant} concentration. At the depths where the ΔC_{ant} is bigger than the ΔDIC, a decrease in biological processes took the overhand which resulted in a less high increase, this happens mainly in the surface waters. At the depth where ΔDIC is bigger than ΔC_{ant} the remineralization of organic matter increased. Another reason for the deviations from the C_{ant} line could be the seasonality and yearly varying DIC concentration in the surface water. The cruises in 1972 and 2014 happened in December and January respectively, so this seasonality should be largely canceled out.

5.4.2 Sensitivity

As the DIC concentration changes upon the addition of C_{ant} to the surface ocean, other parameters in the carbonate system also change. Natural processes that alter for example the pH are a result of changes in thermodynamic drivers and biological processes that (indirectly) affect the pH (Lauvset et al., 2020). These natural processes can alter the anthropogenic influence on the pH changes in the ocean by creating areas that are more or less sensitive to additional changes in pH. Organic matter remineralization affects the pH the most (Lauvset et al., 2020). In the depth range where the products of organic matter remineralization are naturally high, the DIC concentration is also high. This leads to a decreased TA/DIC ratio at this depth, and thus a higher sensitivity for changes in pH at this depth. On top of this, the temperature decreases with depth, leading to naturally lower pH values.

Figure 24 shows that about 100% of the increase in DIC can be related to the addition of C_{ant} to the surface ocean. The small deviations of the ΔDIC line from the ΔC_{ant} line can be related to alterations in the biological pump. Figure 25 shows several other parameters of the carbonate system and they

all seem to react in a similar way to the increase in C_{ant} over time, even though the variation is less pronounced for the other parameters. The maximum difference in -ΔpH, ΔpCO_2 and ΔH^+ is found in the subsurface. This can be related to the increased sensitivity of these parameters at this depth range as a result of the increased remineralization of organic matter on top of the C_{ant} increase. The lower increase in the other variables in the upper 150m shows that the C_{ant} increase affects these parameters less and that they are more affected by changes in the biological pump. Deeper than ~150m all parameters react in a similar way to the C_{ant} increase. The variability mainly in the upper 50m may also be related to regional differences in the surface processes. Seasonality might also play an important part in this upper region.

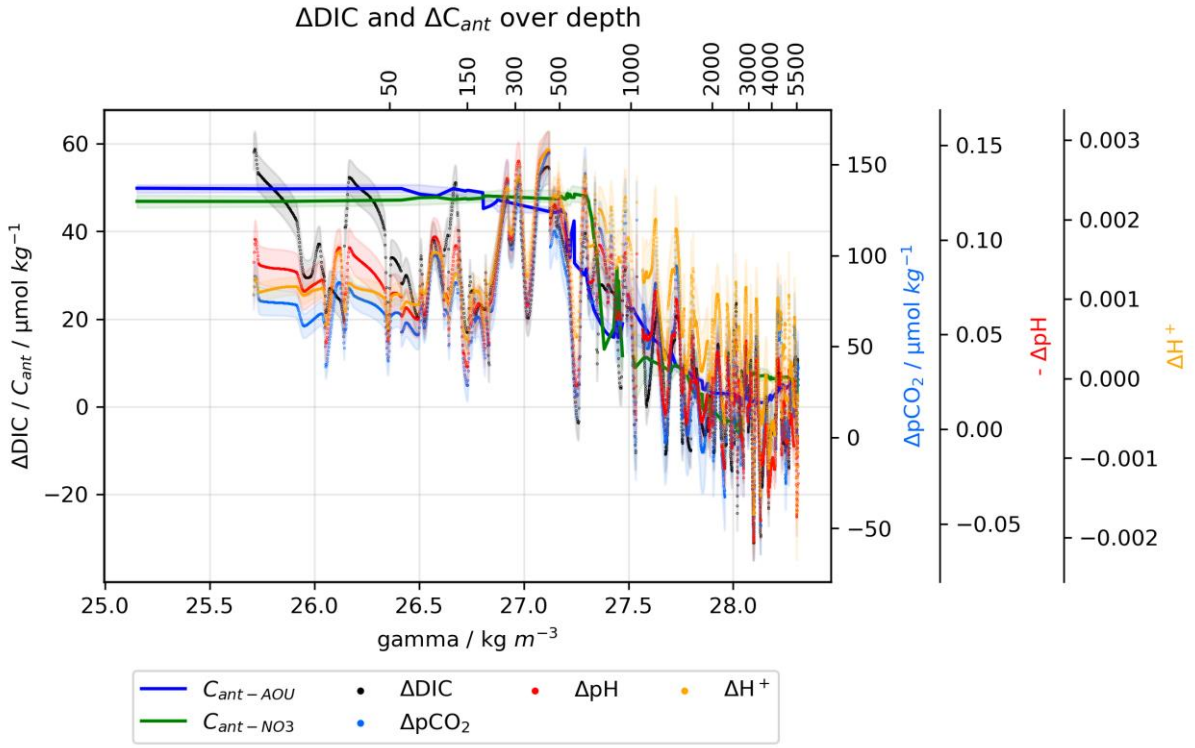

Figure 26: The DIC, pCO2, pH and H+ concentrations of the first years subtracted from the last year plotted together with the C_{ant}

Arroyo et al. (2022) found dissimilar sensitivities to the C_{ant} penetration of different parameters in the carbonate system in the North Pacific Ocean. They found that the maximum change in pCO_2 and H^+ is not at the surface but at a subsurface level around 500m depth, where the products of organic matter remineralization are high and therefore the sensitivity to changes in DIC. The other parameters they investigated, the pH and the Ω_{ar} are highest at the surface and decrease with depth, they follow the distribution of C_{ant} with depth. At this transect the ΔDIC mainly follows the C_{ant} distribution with depth, while the biological pump has big influence on the other parameters in the upper 500m, by creating areas in that are more or less sensitive to changes in C_{anr}. Deeper than that all parameters follow the same trend.

The physical processes altering the C_{ant} concentration are well understood but the role biology plays in influencing the air-water CO_2 exchange and how this might change upon changes in ocean circulation is still mainly unexplored. An in-situ study by Ostle et al. (2022) in the North Atlantic Ocean that investigated phytoplankton abundance and community structure to get a better understanding on the biological influence on the oceanic CO_2 sink. The efficiency of a plankton community is regulated by the community composition, the latitude (the biomass is increasing in the

subpolar North Atlantic, while the biomass decreases in the subtropics) and large scale processes. This increase in biomass in the sub-polar region is happening next to the increasing uptake of C_{ant} in the North Atlantic, increases in temperature and changing ventilation. As the transect at 40°S is located in a biologically very active region in the South Atlantic, it is significant to investigate the role phytoplankton play in regulating the climate. To do this more in-situ phytoplankton studies are needed.

It has become clear that changes in anthropogenic carbon happen on top of the processes leading to the natural DIC distribution with depth. C_{ant} is added to the ocean at the surface and is transported to the internal ocean, while most of the natural DIC is added through the soft tissue pump. At the depth where the soft tissue pump is most active and the input of C_{ant} is high, the extra addition of DIC leads to an increased sensitivity which strengthens the original decrease in pH and increase in H^+ and pCO_2 concentration, caused by the C_{ant} infiltration at the surface.

Revelle factor

As explained before, the Revelle factor is the relative change of CO_2 over the relative change in DIC in a water mass. Upon addition of CO_2 to the ocean the Revelle factor will increase because the CO_2 system equilibria will shift and the pH will decrease consequently. This is why the Revelle Factor is naturally high in the depth range where the products of organic matter remineralization are high. Figure 26 shows that the peak in Revelle Factor has shallowed and the depth range in which the Revelle Factor peaks has become wider. From the surface down to a neutral density level of ~27.5 the Revelle Factor has increased, this is the depth range in which the C_{ant} has intruded. A steep decrease is visible after the peak, this is again the transition from AAIW to NADW. The difference between the peak and the surface water Revelle Factor had decreased, meaning that the natural distribution of the Revelle Factor is slowly disappearing. This part of the water column will take up less CO_2 in the future.

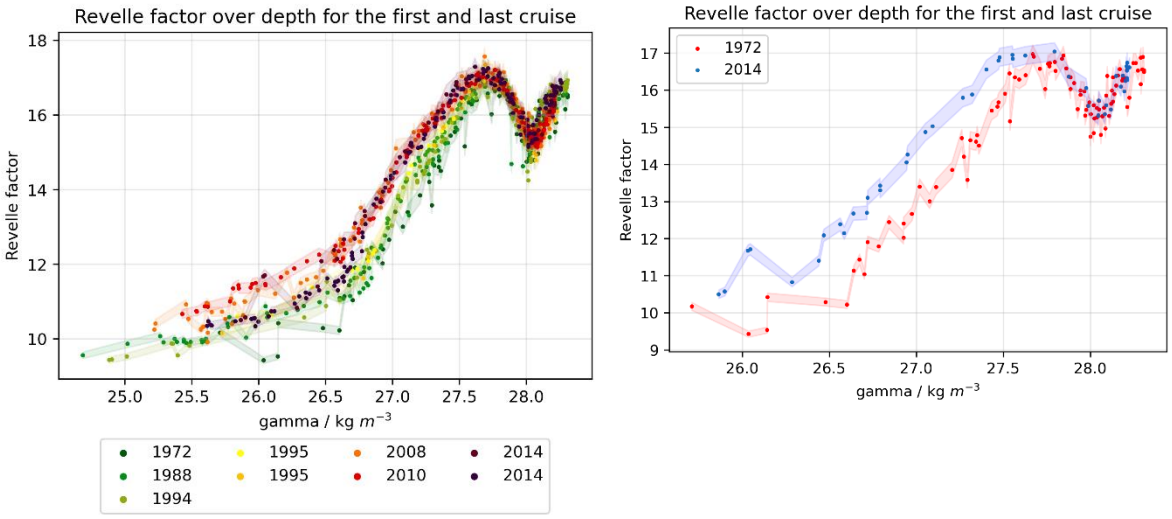

Figure 26: The increase in Revelle Factor over time plotted against neutral density

Conclusion

The surface of the water column is ventilated on a sub-decadal basis, leading to a homogenous C_{ant} concentration in the upper part of the water column. The C_{ant} concentration decreases rapidly with depth, most of the C_{ant} is found in the AAIW. The Revelle Factor has increased in the depth range where C_{ant} has penetrated, leading to a lower buffer value in the surface ocean and thus a less efficient uptake of C_{ant} in this depth range.

Most of the increase in DIC over the period 1972-2014 can be related to the increase in C_{ant} concentration. Natural processes in the ocean create areas in the water column that are more or less sensitive to additional increases in the DIC concentration. The subsurface peak in -ΔpH, ΔpCO_2 and ΔH^+ can be related to the increased sensitivity of these parameters at this depth range. The products of organic matter remineralization led to a decreased TA/DIC ratio, increasing the sensitivity of those variables. This shows that these parameters show similar sensitivities to the increasing anthropogenic carbon concentration in combination with the biological pump.

Appendices

Appendix 1. The complete equation for alkalinity

$TA = [HCO_3^-] + 2[CO_3^{2-}] + [B(OH)_4^-] + [OH^-] + [HPO_4^{2-}] + 2[PO_4^{3-}] + [H_3SiO_4^-] + [NH_3] + [HS^-] - [H^+]_F - [HSO_4^-] - [HF] - [H_3PO_4]$

Zeebe and Wolf-Gladrow, 2001

Appendix 2. Methods

In the original plan for this research new data on the transect were supposed to be collected in January 2023. Due to unfortunate ship problems with a broken engine, the cruise could not sail to the location of the transect but samples were collected at another location in the Atlantic Ocean. Some measurements were done onboard and they will be described in the following paragraphs.

Sampling

The following sampling and analysis methods were performed on one cruise, it is expected that similar methods were performed on the other cruises that were used during the analysis.

All samples were collected in Niskin bottles that were attached to a stainless steel CTD rosette containing 24 bottles. At every station the rosette was lowered to depth and the bottles were filled, as many as possible bottles for different analysis types were filled, depending on how many types of analysis needed to happen to the water.

When the Niskin bottle was opened, oxygen was always sampled first to make sure the exposure time to the atmosphere was the shortest possible. Oxygen samples were taken in 120mL bottles, these bottles were filled through silicon tubing following the Winkler method. The tube was inserted all the way to the bottom of the bottle. The bottle and the cap were rinsed three times before filling, the water used to rinse the bottles was caught in a cup to measure the temperature from. To remove potential air bubbles from the tube the tube was pinched while filling. Once the bottle is filled up it is overflown about three times its own volume, after which the tube is gently removed. Directly after that 1 mL of manganese chloride ($MnCl_2$) was added to the bottle, the tip of the tube flowing from the manganese chloride should be fully submerged and it should have reached the shoulder of the bottle. 2 mL of a mixed solution of sodium hydroxide and potassium iodide (NaOH/KIO) was added in the same way after that. The stopper was added to the bottle and a rubber band was bound around the cap to prevent leakage. The bottles were thoroughly shaken and after 15 minutes the bottles were shaken again. Once all the bottles were filled they were stored fully submerged in a dark box for at least 24 hours before analysis.

After oxygen the TA/ DIC, CO_3^{2-} and pH samples were collected in 250 ml boron silicate glass bottles, the samples were collected following the best-practice recommendations (Dickson et al., 2007a). Filling the bottles was again through a pinchable silicon tube. The bottles and caps were rinsed three times before filling and the bottle was overflown about two times its own volume before sealing the bottle with an air-tight stopper. CO_3^{2-} were analyzed within 12 hours after sampling, if there was time to analyze the pH within 12 hours too, the samples were not poisoned. Otherwise, 1% of each bottle's volume was removed and the samples were poisoned with 50µl mercury chloride (II) so the carbonate chemistry would not change anymore. The TA / DIC samples were then stored in a dark box to be analyzed back at NIOZ. The pH and CO_3^{2-} samples were analyzed on board.

Nutrient samples were collected in 60ml syringes that were connected to the Niskin bottle through a silicon tube. The syringes were rinsed three times before filling. After all the syringes were filled, 2 6ml polyethylene vials were filled with sample from the syringe, the vials and caps were rinsed three

times before filling. 1 was for silicate measurements and was stored in the fridge at 4°C in the dark. The other vial was for ammonium, phosphate, nitrate and nitrite analysis and was stored in the freezer at -20°C. Most of the nutrient sampling was done by Ben Cala.

Only a few salinity samples were taken at every station. The salinity samples were collected in 250ml glass bottles with a plastic stopper and a cap. The bottles were rinsed three times before filling them up to the shoulder of the bottle. The inside of the bottle was then dried with paper tissue before the plastic stopper was added to the bottle, this is to prevent salt crystals from forming. The bottles were closed with a screw cap and then stored in a dark box to be analyzed at NIOZ.

Analysis

Dissolved oxygen, pH and carbonate ions were analyzed during the cruise in the NIOZ lab container by spectrophotometry using the Agilent Cary 8454 UV-VIS spectrophotometer.

After at least 24 hours the oxygen samples could be analyzed, first, 1ml of sulfuric acid was added together with a magnetic flea and the bottles were closed with parafilm to prevent further exposure to oxygen. The sample is stirred for a few seconds before it is connected to a peristaltic pump that continuously pumps the sample into the photometric cell. MiliQ water is pumped through the cell in between samples to avoid contamination. When MiliQ is flowing through the tubes bubbles are created that clear any residual sample before starting a new sample.

To calibrate the oxygen results 5 standards with known oxygen concentrations were prepared and analyzed before the samples. The calibration bottles were filled with seawater in the same way as the samples and 1ml of sulfuric acid was added followed by 2 ml of the mixture of sodium hydroxide and potassium iodide and 1 ml of manganese chloride. The bottles were shaken in between the additions. After that 0, 150, 300, 450, and 600 µl of potassium iodide KIO_3 was added to each bottle respectively. A magnetic flea was added straight afterwards and the bottle was sealed with parafilm. The analysis of the standards was the same as with the samples.

The alkalinity was analyzed using the VINDTA (Versatile Instrument for the Determination of Total Alkalinity) connected to a coulometer back at NIOZ by Ben Cala. The samples were warmed up to 25°C in a warming bath before and during the analysis. The larger of the two pipettes receives approximately 100ml of sample and pushes it into the Titrino cell, where small increments of HCl are titrated into the solution. For this alkalinity titration, an electrode is used to measure the electromotive force. The TA is equal to the total volume of acid needed to reach the equivalence point of carbonic acid.

The very first and last samples of an analysis day are measured in Certified Reference Material (CRM) from A. G. Dickson and every 5 samples a NUTS lab standard was measured to calibrate the data.

The DIC was measured spectrophotometrically with a QuAAtro instrument back at NIOZ. The sample continuously flowed through the analyzer and it was first acidified to a pH <1 and an indicator dye was added (phenolphthalein). This causes the carbonate system equilibria to shift and all the DIC will be in the form of CO_2(g). The CO_2 gas is then pushed over a semipermeable membrane that absorbs the gas and removes the color of the indicator. The color is measured in the flow cell at a wavelength of 550 nm. The change in color can be used to calculate the DIC concentration in combination with measuring a series of standards.

The analytical procedure for pH analysis by spectrophotometry is based on Clayton and Byrne (1993) method and follows the guide to best practices for ocean CO2 measurement (Dickson et al., 2007). The samples were transferred into spectrophotometer glass cells with as little as possible contact

with the atmosphere. Once filled, the cells were closed with stoppers to prevent gas exchange and placed in an aluminum warming box attached to a water bath where the water circulated maintaining the temperature at 25± 0.2°C. Once all the cells are filled, every cell is placed in the cell holder on the spectrophotometer and a reference spectrum is recorded, then 10 µl of m-Cresol Purple is added to the cell and up to 5 absorbances spectra are recorded until the results fall within the preferred range. The pH is calculated with an average of those absorbances.

Carbonate analysis is similar to pH analysis, only here lead perchlorate tetrahydrate is added to the samples and the wavelength of the light was different. This leads to the complexation of lead carbonate which can be measured through spectrophotometric observations. The carbonate ion concentration is calculated from the absorbances.

Appendix 3. C_{ant} compared to pCO_2 in the atmosphere

Figure 1 shows the increase in anthropogenic carbon in the ocean at 40°S together with the increase in the atmospheric CO_2 concentration. The increase in the AAIW was plotted together with the increase in the upper 3000m of the water column. This was done because the C_{ant} concentration has already dropped to zero within the AAIW in many years, so adding the NADW is not necessary to see the carbon signal. Moreover, the NADW contains a wide spread in C_{ant} values (mainly in $C_{ant\text{-}NO3}$) with (unrealistic) peaks in the upper part, that lead to values (far) above and below the C_{ant} values in the AAIW. Except for the first year and 2012, both $C_{ant\text{-}NO3}$ values fall within each other's error ranges. This would be expected taking into account the data from Caínzos et al. (2022), who found that the NADW carries a small part of the C_{ant}, and that the concentrations should fall close together.

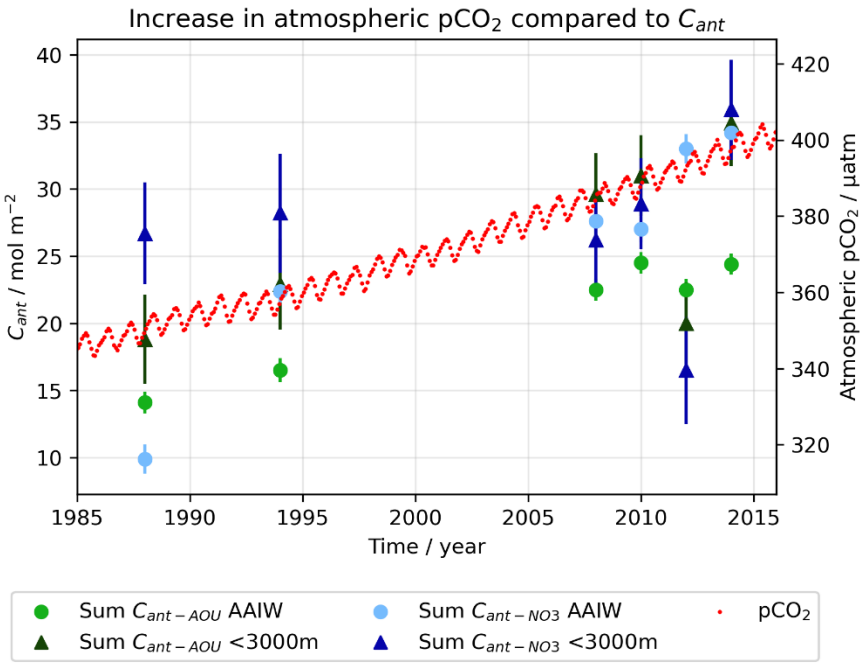

Figure 1: The atmospheric CO_2 concentration increase with time, plotted together with the $C_{ant\text{-}AOU}$ and $C_{ant\text{-}NO3}$ column inventories calculated for just the AAIW and the upper 3000m

The AAIW $C_{ant\text{-}NO3}$ values are higher than the $C_{ant\text{-}AOU}$ values because the $C_{ant\text{-}NO3}$ has a subsurface peak (Figure 19), while the $C_{ant\text{-}AOU}$ only decreases with depth (Figure 20). $C_{ant\text{-}NO3}$ AAIW follows the trend that is predicted by Müller et al. (2023), which is that the carbon sink in the South Atlantic Ocean is becoming more efficient with time: the last two points are plotted above the anthropogenic carbon

line. The $C_{ant\text{-}AOU}$ AAIW follows an opposite trend: the increase in C_{ant} concentration drops from 2012 onwards. This drop can be explained by the increased Revelle Factor in the surface ocean.

References

7.3 The Carbon Cycle and the Climate System—AR4 WGI Chapter 7: Couplings Between Changes in the Climate System and Biogeochemistry. (n.d.). Retrieved October 5, 2022, from https://archive.ipcc.ch/publications_and_data/ar4/wg1/en/ch7s7-3.html

Arroyo, M. C., Fassbender, A. J., Carter, B. R., Edwards, C. A., Fiechter, J., Norgaard, A., & Feely, R. A. (2022). Dissimilar Sensitivities of Ocean Acidification Metrics to Anthropogenic Carbon Accumulation in the Central North Pacific Ocean and California Current Large Marine Ecosystem. Geophysical Research Letters, 49(15), e2022GL097835. https://doi.org/10.1029/2022GL097835

Beal, L. M., De Ruijter, W. P. M., Biastoch, A., & Zahn, R. (2011). On the role of the Agulhas system in ocean circulation and climate. Nature, 472(7344), Article 7344. https://doi.org/10.1038/nature09983

Berends, C. J., de Boer, B., & van de Wal, R. S. W. (2021). Reconstructing the evolution of ice sheets, sea level, and atmospheric CO_2 during the past 3.6 million years. Climate of the Past, 17(1), 361–377. https://doi.org/10.5194/cp-17-361-2021

Blank, N., & Gruber, N. (2007). Impacts of ocean acidification on shelled pteropods in the Southern Ocean. *Biogeochemistry and pollutant dynamics. Institute of Biogeochemistry and Pollutant Dynamics,*

Blank, N. (n.d.). Impacts of Ocean Acidification on Shelled Pteropods in the Southern Ocean. Retrieved April 6, 2023, from https://www.academia.edu/19031666/Impacts_of_Ocean_Acidification_on_Shelled_Pteropods_in_the_Southern_Ocean

Boudreau, B. P., Middelburg, J. J., & Luo, Y. (2018). The role of calcification in carbonate compensation. Nature Geoscience, 11(12), Article 12. https://doi.org/10.1038/s41561-018-0259-5

Boudreau, B. P., Middelburg, J. J., & Meysman, F. J. R. (2010). Carbonate compensation dynamics. Geophysical Research Letters, 37(3). https://doi.org/10.1029/2009GL041847

Browning, T. J., Bouman, H. A., Moore, C. M., Schlosser, C., Tarran, G. A., Woodward, E. M. S., & Henderson, G. M. (2014). Nutrient regimes control phytoplankton ecophysiology in the South Atlantic. Biogeosciences, 11(2), 463–479. https://doi.org/10.5194/bg-11-463-2014

Caínzos, V., Velo, A., Pérez, F. F., & Hernández-Guerra, A. (2022). Anthropogenic Carbon Transport Variability in the Atlantic Ocean Over Three Decades. Global Biogeochemical Cycles, 36(11), e2022GB007475. https://doi.org/10.1029/2022GB007475

cdiac.ess-dive.lbl.gov | 526: Invalid SSL certificate. (n.d.). Retrieved June 8, 2023, from https://cdiac.ess-dive.lbl.gov/ftp/oceans/Handbook_2007/Guide_all_in_one.pdf

Das, S., & Mangwani, N. (2015). Ocean acidification and marine microorganisms: Responses and consequences. Oceanologia, 57(4), 349–361. https://doi.org/10.1016/j.oceano.2015.07.003

Dickson, A. G. (1981). An exact definition of total alkalinity and a procedure for the estimation of alkalinity and total inorganic carbon from titration data. Deep Sea Research Part A. Oceanographic Research Papers, 28(6), 609–623. https://doi.org/10.1016/0198-0149(81)90121-7

Dissimilar Sensitivities of Ocean Acidification Metrics to Anthropogenic Carbon Accumulation in the Central North Pacific Ocean and California Current Large Marine Ecosystem—Arroyo—2022—Geophysical Research Letters—Wiley Online Library. (n.d.). Retrieved June 13, 2023, from https://agupubs.onlinelibrary.wiley.com/doi/full/10.1029/2022GL097835

Dutkiewicz, S., Morris, J. J., Follows, M. J., Scott, J., Levitan, O., Dyhrman, S. T., & Berman-Frank, I. (2015). Impact of ocean acidification on the structure of future phytoplankton communities. Nature Climate Change, 5(11), Article 11. https://doi.org/10.1038/nclimate2722

Enhanced biological carbon consumption in a high CO2 ocean | Nature. (n.d.). Retrieved October 10, 2022, from https://www.nature.com/articles/nature06267

Fassbender, A. J., Orr, J. C., & Dickson, A. G. (2020). Technical note: Interpreting pH changes [Preprint]. Earth System Science/Response to Global Change: Climate Change. https://doi.org/10.5194/bg-2020-348

Figure 6.1 Schematic of the global carbon cycle. (n.d.). Retrieved November 18, 2022, from https://www.pmel.noaa.gov/co2/file/Fig+6.1+Schematic+of+the+global+carbon+cycle

Fu, W., Randerson, J. T., & Moore, J. K. (2016). Climate change impacts on net primary production (NPP) and export production(EP) regulated by increasing stratification and phytoplankton communitystructure in the CMIP5 models. Biogeosciences, 13(18), 5151–5170. https://doi.org/10.5194/bg-13-5151-2016

GEBCO Compilation Group (2023) GEBCO 2023 Grid (doi:10.5285/f98b053b-0cbc-6c23-e053-6c86abc0af7b)

Giresse, P. (2007). Tropical and sub-tropical West Africa—Marine and continental changes during the Late Quaternary. Elsevier.

Gruber, N., Clement, D., Carter, B. R., Feely, R. A., van Heuven, S., Hoppema, M., Ishii, M., Key, R. M., Kozyr, A., Lauvset, S. K., Lo Monaco, C., Mathis, J. T., Murata, A., Olsen, A., Perez, F. F., Sabine, C. L., Tanhua, T., & Wanninkhof, R. (2019). The oceanic sink for anthropogenic CO2 from 1994 to 2007. Science, 363(6432), 1193–1199. https://doi.org/10.1126/science.aau5153

Gruber, N., Friedlingstein, P., Field, C., Valentini, R., Heimann, M., Richey, J., Romero-Lankao, P., Ernst Detlef, S., & Chen, C.-T. A. (2004). The vulnerability of the carbon cycle in the 21st century: An assessment of carbon-climate-human interactions. In The global carbon cycle, 45-76 (2004) (pp. 45–76).

Hoppema, M., Roether, W., Bellerby, R. G. J., & de Baar, H. J. W. (2001). Direct measurements reveal insignificant storage of anthropogenic CO2 in the Abyssal Weddell Sea. Geophysical Research Letters, 28(9), 1747–1750. https://doi.org/10.1029/2000GL012443

Houghton, R. A., & Nassikas, A. A. (2017). Global and regional fluxes of carbon from land use and land cover change 1850–2015. Global Biogeochemical Cycles, 31(3), 456–472. https://doi.org/10.1002/2016GB005546

Humphreys, M. P., Daniels, C. J., Wolf-Gladrow, D. A., Tyrrell, T., & Achterberg, E. P. (2018). On the influence of marine biogeochemical processes over CO2 exchange between the atmosphere and ocean. Marine Chemistry, 199, 1–11. https://doi.org/10.1016/j.marchem.2017.12.006

Humphreys, M. P., Schiller, A. J., Sandborn, D. E., Gregor, L., Pierrot, D., van Heuven, S. M. A. C., Lewis, E. R., and Wallace, D. W. R. (2022). PyCO2SYS: marine carbonate system calculations in Python. *Zenodo.* doi:10.5281/zenodo.3744275

Jacob, D. J. (1999). Introduction to Atmospheric Chemistry. Princeton University Press.

Jones, R. L., Meredith, M. P., Lohan, M. C., Woodward, E. M. S., Van Landeghem, K., Retallick, K., Flanagan, O., Vora, M., & Annett, A. L. (2023). Continued glacial retreat linked to changing macronutrient supply along the West Antarctic Peninsula. Marine Chemistry, 251, 104230. https://doi.org/10.1016/j.marchem.2023.104230

Liu, M., & Tanhua, T. (2021). Water masses in the Atlantic Ocean: Characteristics and distributions. Ocean Science, 17(2), 463–486. https://doi.org/10.5194/os-17-463-2021

Meredith, M. P., Woodworth, P. L., Chereskin, T. K., Marshall, D. P., Allison, L. C., Bigg, G. R., Donohue, K., Heywood, K. J., Hughes, C. W., Hibbert, A., Hogg, A. McC., Johnson, H. L., Jullion, L., King, B. A., Leach, H., Lenn, Y.-D., Morales Maqueda, M. A., Munday, D. R., Naveira Garabato, A. C., … Sprintall, J. (2011). Sustained Monitoring of the Southern Ocean at Drake Passage: Past Achievements and Future Priorities. Reviews of Geophysics, 49(4). https://doi.org/10.1029/2010RG000348

Moore, C. M., Mills, M. M., Arrigo, K. R., Berman-Frank, I., Bopp, L., Boyd, P. W., Galbraith, E. D., Geider, R. J., Guieu, C., Jaccard, S. L., Jickells, T. D., La Roche, J., Lenton, T. M., Mahowald, N. M., Marañón, E., Marinov, I., Moore, J. K., Nakatsuka, T., Oschlies, A., … Ulloa, O. (2013). Processes and patterns of oceanic nutrient limitation. Nature Geoscience, 6(9), Article 9. https://doi.org/10.1038/ngeo1765

Ocean Biogeochemical Dynamics. (2006). https://press.princeton.edu/books/hardcover/9780691017075/ocean-biogeochemical-dynamics

Ostle, C., Landschützer, P., Edwards, M., Johnson, M., Schmidtko, S., Schuster, U., Watson, A. J., & Robinson, C. (2022). Multidecadal changes in biology influence the variability of the North Atlantic carbon sink. Environmental Research Letters, 17(11), 114056. https://doi.org/10.1088/1748-9326/ac9ecf

Dr. Pieter Tans, NOAA/GML (gml.noaa.gov/ccgg/trends/) and Dr. Ralph Keeling, Scripps Institution of Oceanography (scrippsco2.ucsd.edu/)

Price, N., Hamilton, S., Tootell, J., & Smith, J. (2011). Species-specific consequences of ocean acidification for the calcareous tropical green algae Halimeda. Marine Ecology Progress Series, 440, 67–78. https://doi.org/10.3354/meps09309

Rahmstorf, S. (2003). Thermohaline circulation: The current climate. Nature, 421(6924), Article 6924. https://doi.org/10.1038/421699a

Redfield, A. C., Ketchum, B. H., & Richards, F. A. (1963). The influence of organisms on the composition of sea-water. The Sea: Ideas and Observations on Progress in the Study of the Seas. https://www.vliz.be/en/imis?module=ref&refid=28944&printversion=1&dropIMIStitle=1

Riebesell, U., Schulz, K. G., Bellerby, R. G. J., Botros, M., Fritsche, P., Meyerhöfer, M., Neill, C., Nondal, G., Oschlies, A., Wohlers, J., & Zöllner, E. (2007). Enhanced biological carbon consumption in a high CO2 ocean. Nature, 450(7169), Article 7169. https://doi.org/10.1038/nature06267

Ritchie, H., Roser, M., & Rosado, P. (2020). CO_2 and Greenhouse Gas Emissions. Our World in Data. https://ourworldindata.org/co2-emissions

Sarmiento, J. L. (2013). Ocean Biogeochemical Dynamics. In Ocean Biogeochemical Dynamics. Princeton University Press. https://doi.org/10.1515/9781400849079

Sarmiento, Jorge L., and Nicolas Gruber. "Carbon Cycle, CO2, and Climate." In *Ocean Biogeochemical Dynamics*, 392–458. Princeton University Press, 2006. https://doi.org/10.2307/j.ctt3fgxqx.14.

Saunders, P. M., & King, B. A. (1995). Oceanic Fluxes on the WOCE A11 Section. Journal of Physical Oceanography, 25(9), 1942–1958. https://doi.org/10.1175/1520-0485(1995)025<1942:OFOTWA>2.0.CO;2

Schloss, I. R., Abele, D., Moreau, S., Demers, S., Bers, A. V., González, O., & Ferreyra, G. A. (2012). Response of phytoplankton dynamics to 19-year (1991–2009) climate trends in Potter Cove (Antarctica). Journal of Marine Systems, 92(1), 53–66. https://doi.org/10.1016/j.jmarsys.2011.10.006

Sigman, D. M., & Hain, M. P. (2012). The Biological Productivity of the Ocean. 3(6), 16.

SStoll, M. H. C., Bakker, K., Nobbe, G. H., & Haese, R. R. (2001). Continuous-Flow Analysis of Dissolved Inorganic Carbon Content in Seawater. Analytical Chemistry, 73(17), 4111–4116. https://doi.org/10.1021/ac010303r Stoll, M. H. C., Bakker, K., Nobbe, G. H., & Haese, R. R. (2001). Continuous-Flow Analysis of Dissolved Inorganic Carbon Content in Seawater. *Analytical Chemistry*, *73*(17), 4111–4116. https://doi.org/10.1021/ac010303r

Takahashi, T., Sutherland, S. C., Chipman, D. W., Goddard, J. G., Ho, C., Newberger, T., Sweeney, C., & Munro, D. R. (2014). Climatological distributions of pH, pCO2, total CO2, alkalinity, and CaCO3 saturation in the global surface ocean, and temporal changes at selected locations. Marine Chemistry, 164, 95–125. https://doi.org/10.1016/j.marchem.2014.06.004

Takahashi, T., Sutherland, S. C., Wanninkhof, R., Sweeney, C., Feely, R. A., Chipman, D. W., Hales, B., Friederich, G., Chavez, F., Sabine, C., Watson, A., Bakker, D. C. E., Schuster, U., Metzl, N., Yoshikawa-Inoue, H., Ishii, M., Midorikawa, T., Nojiri, Y., Körtzinger, A., … de Baar, H. J. W. (2009). Climatological mean and decadal change in surface ocean pCO2, and net sea–air CO2 flux over the global oceans. Deep Sea Research Part II: Topical Studies in Oceanography, 56(8), 554–577. https://doi.org/10.1016/j.dsr2.2008.12.009

Talley, L. D. (1996). Antarctic Intermediate Water in the South Atlantic. In G. Wefer, W. H. Berger, G. Siedler, & D. J. Webb (Eds.), The South Atlantic: Present and Past Circulation (pp. 219–238). Springer. https://doi.org/10.1007/978-3-642-80353-6_11

Talley, L. D. (2011). Descriptive Physical Oceanography: An Introduction. Academic Press.

Talley, L. D., Pickard, G. L., Emery, W. J., & Swift, J. H. (2011). Chapter 9—Atlantic Ocean. In L. D. Talley, G. L. Pickard, W. J. Emery, & J. H. Swift (Eds.), Descriptive Physical Oceanography (Sixth Edition) (pp. 245–301). Academic Press. https://doi.org/10.1016/B978-0-7506-4552-2.10009-5

Toggweiler, J. R., & Russell, J. (2008). Ocean circulation in a warming climate. Nature, 451(7176), Article 7176. https://doi.org/10.1038/nature06590

Total alkalinity: The explicit conservative expression and its application to biogeochemical processes—ScienceDirect. (n.d.). Retrieved November 21, 2022,

from https://www.sciencedirect.com/science/article/pii/S0304420307000047?casa_token=pkc_I4rakYoAAAAA:PPW9VBOxhFtEIo9bP14BAvqG6ScTJkhZ0MtPTSsvynecEGmIFIv-05_EDD17U9n1xEnlvVhzI85k

US Department of Commerce, N. (n.d.-a). Global Monitoring Laboratory—Carbon Cycle Greenhouse Gases. Retrieved October 5, 2022, from https://gml.noaa.gov/ccgg/trends/global.html

US Department of Commerce, N. (n.d.-b). Global Monitoring Laboratory—Carbon Cycle Greenhouse Gases. Retrieved March 10, 2023, from https://gml.noaa.gov/ccgg/trends/

van Heuven, S. M. A. C., Hoppema, M., Huhn, O., Slagter, H. A., & de Baar, H. J. W. (2011). Direct observation of increasing CO2 in the Weddell Gyre along the Prime Meridian during 1973–2008. Deep Sea Research Part II: Topical Studies in Oceanography, 58(25), 2613–2635. https://doi.org/10.1016/j.dsr2.2011.08.007

Walker, N. D. (1986). Satellite observations of the Agulhas Current and episodic upwelling south of Africa. Deep Sea Research Part A. Oceanographic Research Papers, 33(8), 1083–1106. https://doi.org/10.1016/0198-0149(86)90032-4

Wanninkhof, R., Asher, W. E., Ho, D. T., Sweeney, C., & McGillis, W. R. (2009). Advances in Quantifying Air-Sea Gas Exchange and Environmental Forcing. Annual Review of Marine Science, 1(1), 213–244. https://doi.org/10.1146/annurev.marine.010908.163742

Wohlers, J., Engel, A., Zöllner, E., Breithaupt, P., Jürgens, K., Hoppe, H.-G., Sommer, U., & Riebesell, U. (2009). Changes in biogenic carbon flow in response to sea surface warming. Proceedings of the National Academy of Sciences, 106(17), 7067–7072. https://doi.org/10.1073/pnas.0812743106

Wolf-Gladrow, D. A., Zeebe, R. E., Klaas, C., Körtzinger, A., & Dickson, A. G. (2007). Total alkalinity: The explicit conservative expression and its application to biogeochemical processes. Marine Chemistry, 106(1–2), 287–300. https://doi.org/10.1016/j.marchem.2007.01.006

Wunsch, C. (2002). What Is the Thermohaline Circulation? Science, 298(5596), 1179–1181. https://doi.org/10.1126/science.1079329

Yamamoto, A., Abe-Ouchi, A., & Yamanaka, Y. (2018). Long-term response of oceanic carbon uptake to global warming via physical and biological pumps. Biogeosciences, 15(13), 4163–4180. https://doi.org/10.5194/bg-15-4163-2018

Zeebe, R. E., & Wolf-Gladrow, D. (2001). CO2 in Seawater: Equilibrium, Kinetics, Isotopes. Gulf Professional Publishing.

Zickfeld, K., Eby, M., & Weaver, A. J. (2008). Carbon-cycle feedbacks of changes in the Atlantic meridional overturning circulation under future atmospheric CO2. Global Biogeochemical Cycles, 22(3). https://doi.org/10.1029/2007GB003118